OPEN ACCESS

ORIGINAL RESEARCH

Mitochondrial impairment drives intestinal stem cell transition into dysfunctional Paneth cells predicting Crohn's disease recurrence

Sevana Khaloian,[1] Eva Rath ,[1] Nassim Hammoudi,[2] Elisabeth Gleisinger,[1] Andreas Blutke,[3] Pieter Giesbertz,[4] Emanuel Berger,[1] Amira Metwaly,[1] Nadine Waldschmitt,[1] Matthieu Allez ,[2] Dirk Haller [1,5]

► Additional material is published online only. To view please visit the journal online (http://dx.doi.org/10.1136/gutjnl-2019-319514).

For numbered affiliations see end of article.

Correspondence to
Professor Dirk Haller, Chair of Nutrition and Immunology, Technische Universität München, München, Bayern 85350, Germany; dirk.haller@tum.de

SK and ER contributed equally.

Received 20 July 2019
Revised 23 January 2020
Accepted 3 February 2020
Published Online First 28 February 2020

ABSTRACT

Objective Reduced Paneth cell (PC) numbers are observed in inflammatory bowel diseases and impaired PC function contributes to the ileal pathogenesis of Crohn's disease (CD). PCs reside in proximity to Lgr5^{+} intestinal stem cells (ISC) and mitochondria are critical for ISC-renewal and differentiation. Here, we characterise ISC and PC appearance under inflammatory conditions and describe the role of mitochondrial function for ISC niche-maintenance.

Design Ileal tissue samples from patients with CD, mouse models for mitochondrial dysfunction (Hsp60$^{\Delta/\Delta ISC}$) and CD-like ileitis (TNF$^{\Delta ARE}$), and intestinal organoids were used to characterise PCs and ISCs in relation to mitochondrial function.

Results In patients with CD and TNF$^{\Delta ARE}$ mice, inflammation correlated with reduced numbers of Lysozyme-positive granules in PCs and decreased *Lgr5* expression in crypt regions. Disease-associated changes in PC and ISC appearance persisted in non-inflamed tissue regions of patients with CD and predicted the risk of disease recurrence after surgical resection. ISC-specific deletion of Hsp60 and inhibition of mitochondrial respiration linked mitochondrial function to the aberrant PC phenotype. Consistent with reduced stemness in vivo, crypts from inflamed TNF$^{\Delta ARE}$ mice fail to grow into organoids ex vivo. Dichloroacetate-mediated inhibition of glycolysis, forcing cells to shift to mitochondrial respiration, improved ISC niche function and rescued the ability of TNF$^{\Delta ARE}$ mice-derived crypts to form organoids.

Conclusion We provide evidence that inflammation-associated mitochondrial dysfunction in the intestinal epithelium triggers a metabolic imbalance, causing reduced stemness and acquisition of a dysfunctional PC phenotype. Blocking glycolysis might be a novel drug target to antagonise PC dysfunction in the pathogenesis of CD.

Significance of this study

What is already known on this subject?

- Reduced Paneth cell (PC) numbers are frequently observed in inflammatory bowel diseases (IBD) and impaired PC function is a feature of ileal Crohn's disease (CD).
- PCs are involved in mucosal defence and support the intestinal stem cell (ISC) niche.
- Mitochondrial dysfunction and alterations in energy metabolism in general are implicated during the onset and the course of IBD.
- Mitochondrial function, metabolism and mitochondrial unfolded protein response are involved in intestinal epithelial cell differentiation and determine the cellular phenotype.

What are the new findings?

- Reduced expression of the ISC marker *Lgr5*, in addition to reduced PC granularity, correlates with inflammation in patients with CD and CD-like TNF$^{\Delta ARE}$ mice.
- Morphological appearance of PCs and ISC in non-affected tissue margins predicts early postoperative endoscopic recurrence in patients with CD.
- Induction of mitochondrial dysfunction in ISC by Hsp60 loss results in overall reduced *Lgr5* expression and causes differentiation of *Lgr5*$^{+}$ into aberrant PCs.
- Reinforcing mitochondrial respiration by inhibition of glycolysis restores inflammation-imprinted dysfunction of the ISC niche.

How might it impact on clinical practice in the foreseeable future?

- We provide evidence that impaired mitochondrial function is linked to the CD-associated loss of stemness and the generation of dysfunctional PC phenotypes. Demonstrating a proof-of-concept for targeting ISC alterations by implementing a drug-related metabolic shift, we rationalise a novel treatment approach for CD.

INTRODUCTION

Crohn's disease (CD), belonging to the group of inflammatory bowel diseases (IBD), is characterised by transmural acute and chronic inflammation of intestinal tissue regions, typically involving the terminal ileum.[1] In the pathogenesis of CD, multiple genetic risk factors together with environmental triggers result in a disturbed immune response towards a dysbiotic commensal microbiota.[2] The intestinal epithelium as interface between microbiota and host critically contributes to intestinal homeostasis, and alterations in intestinal epithelial

Linked

► http://dx.doi.org/10.1136/gutjnl-2019-319523

Check for updates

To cite: Khaloian S, Rath E, Hammoudi N, *et al*. *Gut* 2020;**69**:1939–1951.

cell (IEC) subtypes including reduced numbers of goblet cells and Paneth cells (PCs) are frequently observed under inflammatory conditions.[3] PCs are located in the crypt base of the small intestine, residing between Leucine-rich repeat-containing G-protein coupled receptor (Lgr) 5 crypt base columnar (CBC) intestinal stem cells (ISCs) and via secretion of antimicrobial peptides (AMPs) such as lysozyme, defensins (cryptdins), angiogenin-4 (Ang4) and secretory phospholipase A2, PCs contribute to pathogen clearance and shape the commensal microbiota.[4 5]

In addition to mucosal defence, PCs provide essential signals for maintenance of the ISC niche. Among those are Notch ligand (Dll4), and secreted factors like EGF and Wnt3,[6] and also more recently identified metabolic signalling molecules including cyclic ADP ribose (cADPR)[7] and lactate,[8] facilitating optimal stem cell function. Moreover, on acute injury, PCs themselves serve as a reserve stem cell population, restoring Lgr5$^+$ ISC via dedifferentiation, thereby contributing to tissue regeneration.[9–11]

Genetic risk variants of prominent CD-relevant genes involved in autophagy (*ATG16L1*), bacterial-sensing (*NOD2*), endoplasmic reticulum (ER) stress response (*XBP1*) and Wnt signalling (*TCF4*) were shown to affect PC function in terms of AMP production and secretion, and loss of PC defensins is particularly associated with ileal phenotypes of CD.[3 12–16] Yet, it is controversial whether ileal CD is a specific disorder of PCs, or if loss of PC function is merely associated, but not causal for the development of CD. IEC-specific knockout models developing CD-like ileal inflammation including Caspase 8$^{-/-}$,[17] Atg16l1$^{-/-}$[15] and Xbp1$^{-/-}$[12] mice share the loss of PC function as a mechanism of pathogenesis; however, genetic ablation of PCs is not sufficient to generate a CD-associated phenotype.[18 19] In line with a role of PCs in disease progression, TNF$^{\Delta ARE}$ mice, a bacterial-driven model of chronic CD-like ileitis, display a loss of lysozyme-positive PCs subsequent to, but not preceding, the onset of TNF-driven tissue pathology. No increase in apoptosis could be observed in crypts from TNF$^{\Delta ARE}$ mice, suggesting epithelial remodelling rather than PC-specific cell death.[20] The cause of PC alterations as well as PC fate under chronic inflammatory conditions is currently unknown, though impairment of the exocytosis pathway in PC of mice with hypomorphic expression of the CD susceptibility gene *Atg16l1* is paralleled by degenerating mitochondria.[14] Interestingly, several genetic risk factors affecting mitochondrial function were identified for IBD,[21] and intestinal inflammation has been suggested as energy-deficiency disease of IECs featuring alterations of the mitochondrial metabolism.[22 23] Concomitantly, mitochondrial function and signalling pathways like the mitochondrial unfolded protein response (MT-UPR) have emerged as cellular checkpoint of metabolism, stemness and IEC differentiation programme.[24] We previously demonstrated MT-UPR activation in IEC from patients with IBD and mouse models of intestinal inflammation[25] and showed that activation of MT-UPR, induced by IEC-specific loss of the mitochondrial chaperone Hsp60, resulted in impaired mitochondrial respiration, and loss of ISC.[26] However, the cellular origin and specific mechanisms that integrate mitochondrial function into CD pathology remain unknown. The cellular metabolism is increasingly recognised as a determiner of cellular phenotype and stem cell fate,[24] and taking the essential role of PCs in the regulation of the ISC niche into account, we aimed at characterising PCs and Lgr5$^+$ ISC in the context of mitochondrial function and inflammation.

In this study, we show that reduced PC granularity and reduced *Lgr5* expression correlate with inflammation in patients with CD and TNF$^{\Delta ARE}$ mice. Importantly, the morphological appearance of the ISC niche in non-affected tissue margins predicts early postoperative endoscopic recurrence in patients with CD, identifying an objective biomarker to select patients for preventive treatment. Induction of mitochondrial dysfunction in ISC by Hsp60 loss results in overall reduced *Lgr5* expression and causes differentiation of *Lgr5*$^+$ into aberrant PCs. Remarkably, inhibition of glycolysis is sufficient to override the inflammation-imprinted changes of the ISC niche ex vivo and rescued the ability of TNF$^{\Delta ARE}$ mice-derived crypts to give rise to organoids.

METHODS AND MATERIAL

All relevant methods and materials can be found in the online supplementary material.

RESULTS

REDUCED PANETH CELL FUNCTION AND *LGR5*-EXPRESSION CORRELATE WITH CD-LIKE INFLAMMATION

In TNF$^{\Delta ARE}$ mice, a deletion in the tumour necrosis factor (TNF) AU-rich (adenosin-uracil) elements (ARE) leads to loss of translational control of TNF, resulting in a microbiota-driven transmural inflammation of the distal ileum.[20] CD-like tissue inflammation gradually develops in TNF$^{\Delta ARE}$ mice and has been linked to PC dysfunction.[20] PCs contain distinct cytoplasmic granules for exocytosis of AMPs,[27] and lysozyme-positive (Lyz$^+$) secretory granule morphology is used as a functional marker for PC phenotype classification.[13 14] We took advantage of the heterogeneity in the grade of CD-like inflammation in TNF$^{\Delta ARE}$ mice to characterise PCs across a broad range of histopathological scores (HS). Ileal tissue sections derived from TNF$^{\Delta ARE}$ mice with no (HS 0), moderate (HS <4) and severe (HS>4) inflammation were stained for Lyz and PCs were subdivided into a highly granular (≥2 Lyz$^+$ cytoplasmic granules) and a lowly granular (<2 Lyz$^+$ cytoplasmic granules and/or diffuse cytoplasmic Lyz staining) phenotype (figure 1A). Representative H&E stainings of tissue sections at different HS are given in figure 1B. Total numbers of Lyz$^+$ PCs per crypt (figure 1C) and the percentage of highly granular PCs (figure 1D) inversely correlated with the grade of inflammation and signs of PC abnormalities were already visible in moderately inflamed mice (figure 1C,D). Comparing tissues from non-inflamed TNF$^{\Delta ARE}$ mice and wild type (WT) littermates, we observed no differences in the total numbers of PCs. However, non-inflamed TNF$^{\Delta ARE}$ mice showed a mild reduction in PC granularity (online supplementary figure 1A,B). Confirming reduced PC function in TNF$^{\Delta ARE}$ mice, transcriptional levels of *Lyz1* and PC-derived AMPs alpha-defensin 5 (*Defa5*) and *Ang4* and ISC-niche supporting *Dll4* were reduced (figure 1E). To depict the impact of ileitis-associated changes in PC function on CBC ISC marked by Lgr5 we performed in situ hybridisation for *Lgr5* (figure 1F). The number of dots, representing *Lgr5* transcripts, were counted (figure 1G) and crypts were classified as crypts with high *Lgr5* expression (≥10 dots) and low *Lgr5* expression (<10 dots), respectively. Consistent with reduced PC function, *Lgr5*$^+$ ISCs were diminished under inflammatory conditions (online supplementary figure 1C) and numbers of crypts with high *Lgr5* expression were inversely correlated with the degree of histopathology (figure 1H). Reduced stemness in inflamed TNF$^{\Delta ARE}$ mice was confirmed by qPCR analysis of *Lgr5* (figure 1I). No differences were observed in crypt morphology and *Lgr5* expression between WT and non-inflamed TNF$^{\Delta ARE}$ mice (online supplementary figure 1C,D). In situ hybridisation for Olfactomedin (Olfm) 4, a broader marker of active ISCs, confirmed reduced stemness under inflammatory conditions (online supplementary figure 1E-G). The

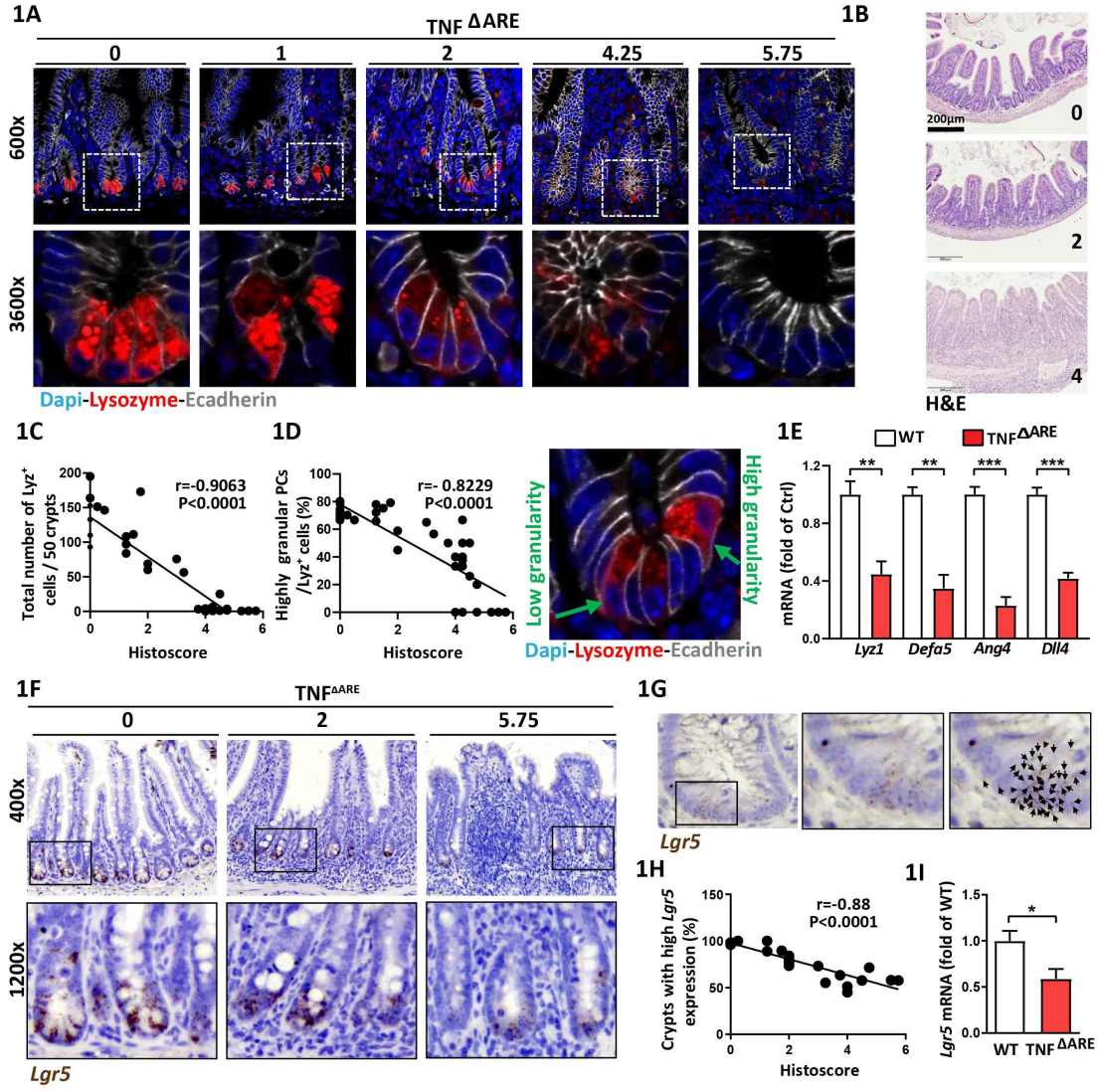

Figure 1 Paneth cell dysfunction and reduced *Lgr5*-expression correlate with CD-like inflammation in TNF$^{\Delta ARE}$ mice Ileal tissue sections from TNF$^{\Delta ARE}$ mice with different levels of inflammation and IEC isolates derived from TNF$^{\Delta ARE}$ mice and WT littermates were analysed. (A) Immunofluorescence (IF) costaining of Lysozyme (red) and E-cadherin (IEC borders, grey) counterstained with Dapi (nuclei, blue), lower panel: higher magnification of the indicated sections. Numbers above the pictures indicate the HS of the respective tissue section. (B) Representative H&E images for HS 0 (non-inflamed), 2 (moderate inflammation), 4 (severe inflammation). (C) Correlation analysis (Pearson) of the number of Lysozyme positive (Lyz$^+$) cells and HS and (D) proportions of highly granular Lyz$^+$ cells (≥2 granules) and HS. Right: representative Lyz staining depicting Lyz$^+$ cells with low and high granularity, respectively. (E) qRT-PCR analysis of IECs for genes involved in PC function (n=5) (F) Representative pictures of *Lgr5 in situ* hybridisation, including magnifications; numbers indicate the respective HS. (G) Illustration of *Lgr5* transcript quantification; each dot, indicated by a black arrow represents one *Lgr5* transcript. (H) Correlation analysis (Pearson) of the proportion of crypts with high *Lgr5* expression (≥10 transcripts) and HS. (I) qRT-PCR analysis of IECs for *Lgr5* (n=5). Statistics were performed by unpaired *t*-test. Bars represent mean+SEM. Asterisks indicate significant differences *p<0.05, **p<0.01, ***p<0.001. ARE,AU-rich (adenosin-uracil) elements; CD, Crohn's disease; HS, histopathological score; IEC, intestinal epithelial cell; PC, Paneth cell; TNF, tumour necrosis factor; WT, wild type.

parallel decrease of PC function and stemness indicates the tight functional interrelation of the ISC niche under inflammatory conditions.

ABERRANT PC PHENOTYPE AND *LGR5*-EXPRESSION CORRELATE WITH ACTIVE ILEAL CD

To verify the relevance of TNF$^{\Delta ARE}$ mice, we obtained samples from 70 patients with CD undergoing surgical resection from a previously published prospective study.[28] Early postoperative lesions observed by ileocolonoscopy best predict the course of disease and ileocolonoscopy is currently the gold standard to assess the risk of clinical recurrence.[29] Ileal tissue margins were collected during resection surgery and a postoperative endoscopy was performed 6–12 months later to assess the endoscopic recurrence according to the Rutgeerts score. Endoscopic recurrence was defined as a Rutgeerts score ≥i2. Classification of patients with CD according to the presence or absence of inflammation in the resected tissue samples at baseline, and classification of postoperative endoscopic recurrence, is schematically shown in figure 2A, and patients' characteristics at the time of surgery are compiled in online supplementary table 1. Consistent with TNF$^{\Delta ARE}$ mice, numbers of LYZ$^+$ PCs and highly granular PCs (≥2 LYZ$^+$ cytoplasmic granules) were significantly reduced in tissue margins classified as inflamed at time of surgery

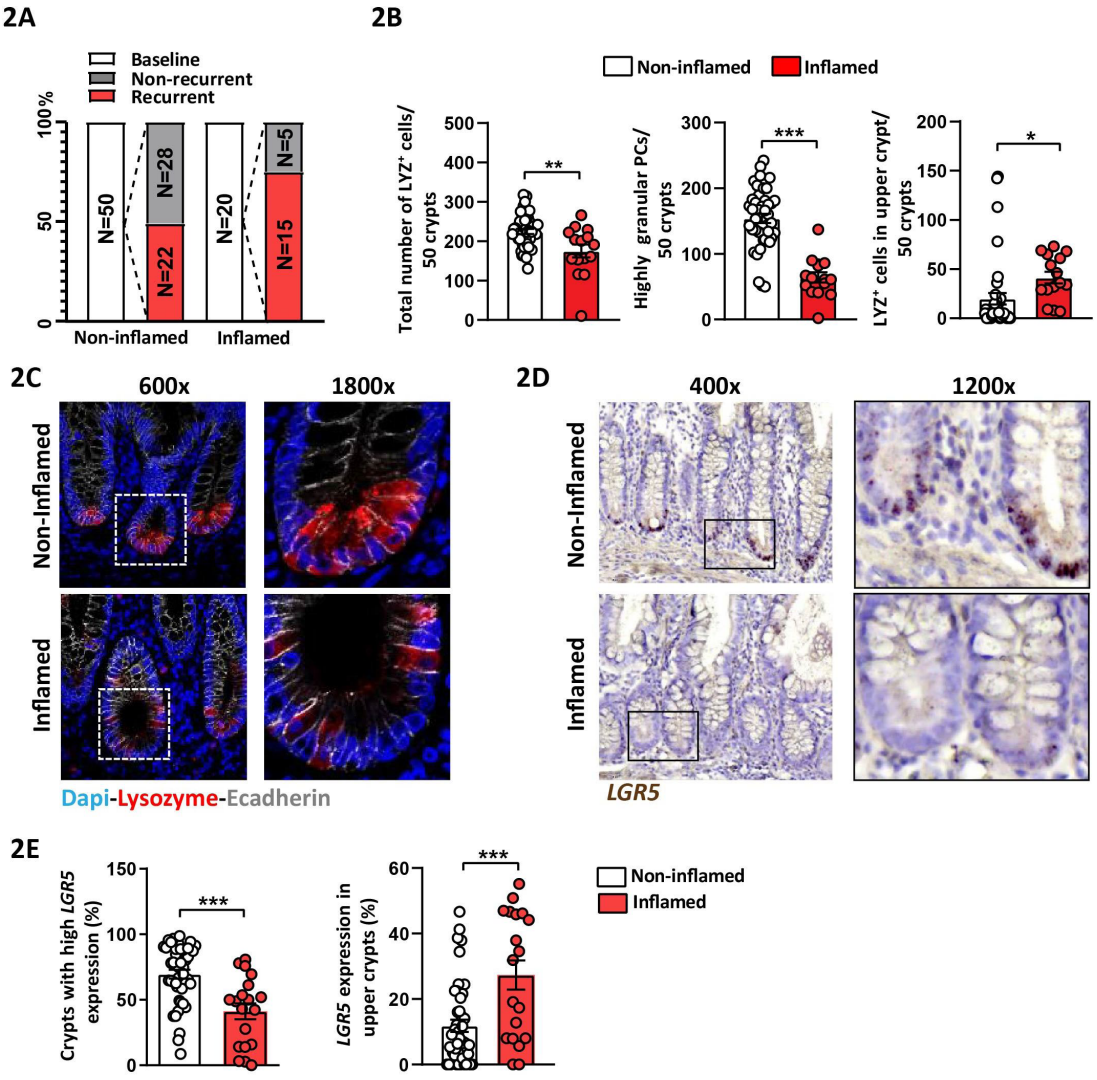

Figure 2 Aberrant Paneth cell phenotype and *LGR5*-expression correlate with disease activity in ileal tissue margins of patients with CD Ileal tissue sections of patients with CD undergoing resection surgery were analysed and tissue margins classified as non-inflamed and inflamed, respectively, at time of surgery were compared. (A) Overview of CD patient numbers for baseline and endoscopic follow-up disease classification. (B) Quantification of the total number of LYZ$^+$ cells, highly granular LYZ$^+$ cells (≥2 granules) and number of LYZ$^+$ cells in upper crypt based on LYZ IF staining. (C) Representative pictures of IF costaining of Lysozyme (red) and E-cadherin (IEC borders, grey) counterstained with Dapi (nuclei, blue), right panel: higher magnification of the indicated sections. (D) Representative pictures of *LGR5 in situ* hybridisation, including magnifications. (E) Quantification of *LGR5 in situ* hybridisation giving the proportion of crypts with high *LGR5* expression (≥15 *LGR5* transcripts) and of crypts with *LGR5* expression in upper crypt. Statistics were performed by unpaired *t*-test. Bars represent mean+SEM. Asterisks indicate significant differences *p<0.05, **p<0.01, ***p<0.001. CD, Crohn's disease; IEC, intestinal epithelial cell; LYZ$^+$, Lysozyme positive.

compared with those classified as non-inflamed (figure 2B,C). Interestingly, the number of LYZ$^+$ cells in 'upper crypt' (above +6 position) significantly increased in inflamed compared with non-inflamed tissue margins, suggesting an aberrant ISC niche architecture under inflammatory conditions (figure 2B, right). Reflecting the CD-like mouse model, inflamed tissue margins displayed a reduction in crypts with high *LGR5* expression (≥15 dots), and concomitant to LYZ$^+$ cells above the +6 position, *LGR5* expression in upper crypts was induced (figure 2D,E).

PANETH CELL PHENOTYPE AND *LGR5*-EXPRESSION PATTERN PREDICT RECURRENCE IN PATIENTS WITH CD

As previously shown,[28] inflammation in resected ileal tissue at baseline was predictive for endoscopic recurrence, yet 44% of the analysed patients with CD with non-inflamed tissue margins still developed recurrent disease (figure 2A). Analysing regions of the intestine free of severe active or chronic inflammation has been proposed to more accurately reflect disease development due to the potential presence of early molecular and pathologic changes.[13] Therefore, we tested in ileal margins classified as non-inflamed at the time of surgery if abnormal PC phenotypes and aberrant *LGR5*$^+$ expression predict endoscopic recurrence after 6–12 months. Indeed, a low proportion of highly granular PCs (figure 3A,B) and high numbers of LYZ$^+$ cells in upper crypts (figure 3C,D) correlated with the risk of recurrence, while the total number of LYZ$^+$ PCs in crypts were not different between recurrent and non-recurrent groups (online supplementary figure 2A,B). In line, a low proportion of crypts with high *LGR5* expression (figure 3E,F) and enhanced *LGR5* expression in upper crypts (figure 3G,H) were further predictive for endoscopic recurrence. Assigning numbers of highly granular PCs, PCs in upper crypt, highly *Lgr5* expressing crypts and *Lgr5* expression in upper crypts as risk factors (0–4), we demonstrated

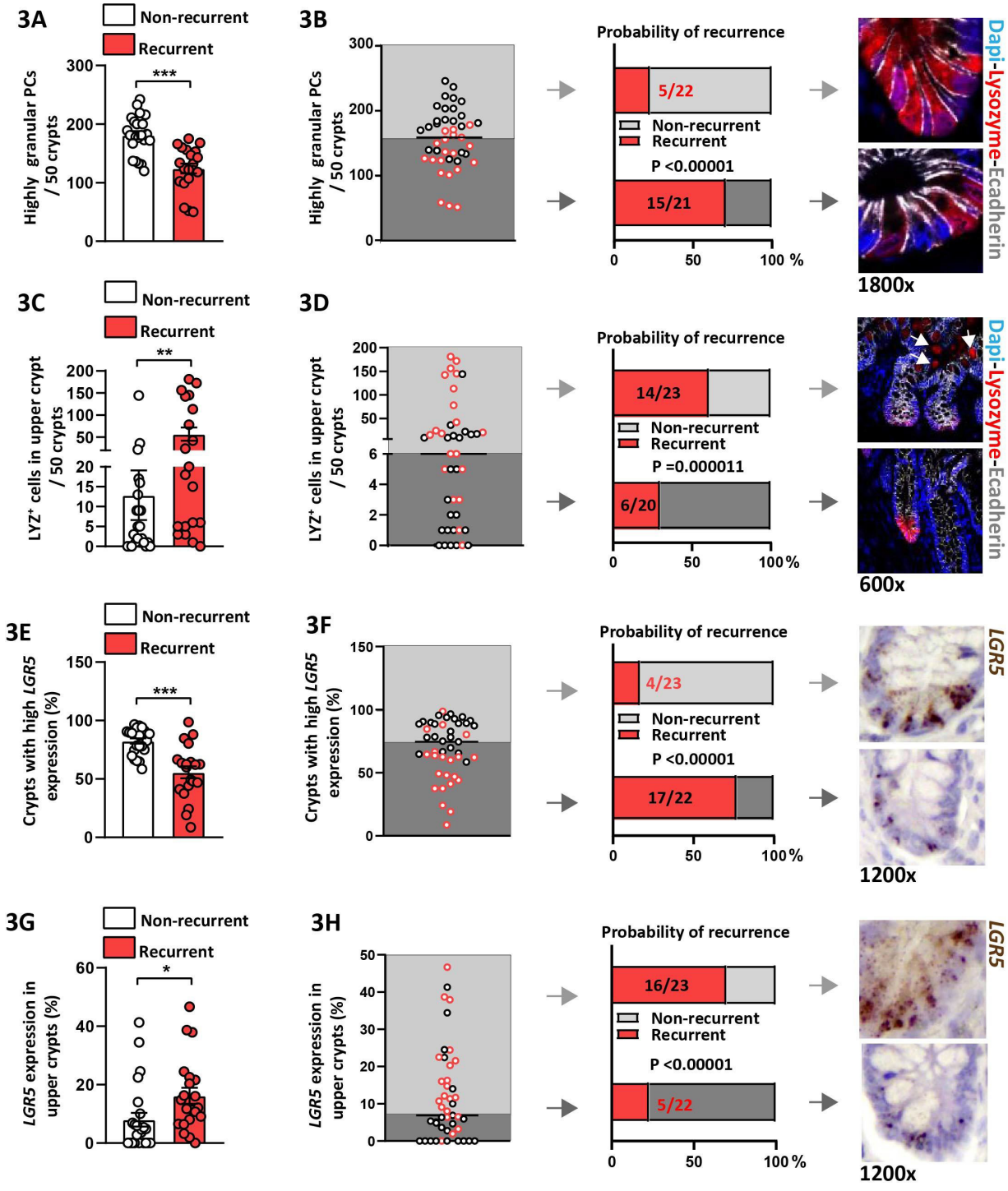

Figure 3 PC phenotype and *LGR5*-expression predict disease recurrence in patients with non-inflamed CD Ileal tissue sections classified as non-inflamed at time of surgery of patients with CD undergoing resection surgery were analysed. Tissue sections were stained for LYZ by IF and for *LGR5* by in situ hybridisation, respectively, and expression patterns were quantified. Numbers of highly granular LYZ$^+$ cells (≥2 granules), numbers of LYZ$^+$ cells in upper crypt, proportion of crypts with high *LGR5* expression (≥15 *LGR5* transcripts) and proportion of crypts with *LGR5* expression in upper crypt were determined. Patients with CD with endoscopic recurrence (Rutgeerts score ≥i2) 6–12 months after surgery were compared with patients with CD not experiencing recurrence. (A,C,E,G) Overall comparison of recurrent versus non-recurrent patients for the respective marker; (B,D,F,H) From left to right: distribution of the respective marker among patients with recurrent (red circles) and non-recurrent (black circles) CD with median indicated; probability of patients with CD to experience recurrence if above or below the median for the respective marker; representative pictures showing sections from patients with CD above or below median. (A,B) Number of highly granular LYZ$^+$ cells (≥2 granules), (C,D) Number of LYZ$^+$ cells in upper crypt, (B,D) IF costainings of Lysozyme (red) and E-cadherin (IEC borders, grey) counterstained with Dapi (nuclei, blue). (E,F) Proportion of crypts with high *LGR5* expression (≥15 *LGR5* transcripts), (G,H) proportion of crypts with *LGR5* expression in upper crypt, (F,H) *LGR5 in situ* hybridisation. (A,C,E,G) Statistics were performed by unpaired *t*-test. Bars represent mean+SEM. Asterisks indicate significant differences *p<0.05, **p<0.01, ***p<0.001. (B,D,F,H) Statistical analysis was performed via χ^2 test. CD, Crohn's disease; IEC, intestinal epithelial cell; LYZ$^+$, Lysozyme positive; PC, Paneth cell.

a strong cumulative effect of the number of risk factors on the probability of disease recurrence (online supplementary figure 2C). Smoking, that had been identified previously as a risk factor for recurrence in this cohort,[28] was associated with reduced PC granularity, a low proportion of crypts with high *LGR5* expression and enhanced *LGR5* expression in upper crypts (online supplementary figure 3A–C). Yet, within patients with CD experiencing recurrence, smoking had no additional impact on the risk factors analysed (online supplementary figure 3D,E). CD-associated risk alleles of NOD2 and ATG16L1 have been reported to impact PC phenotype;[13] however, we observed no impact of the single nucleotide polymorphisms ATG16L1 rs6752107 and NOD2 rs2066845 or rs2066844 on the ISC niche appearance, probably due to a high proportion of risk allele carriers (online supplementary figure 3F-H). Contrarily, in tissue margins classified as inflamed at the time of surgery, aberrant PC phenotypes and stemness failed to better stratify disease recurrence (online supplementary figure 4). In summary, these data show a strong predictive value for alterations of the ISC niche for early endoscopic recurrence, indicating these phenotypic changes as first molecular signs of inflammatory changes, preceding macroscopic lesions.

INFLAMMATION IN TNF$^{\Delta ARE}$ MICE IS ASSOCIATED WITH IMPAIRED MITOCHONDRIAL FUNCTION

Phenotypic changes of PCs have been described concomitantly to structurally impaired mitochondria,[14] and mitochondrial stress signalling (MT-UPR) is apparent in IEC from patients with IBD and mouse models of intestinal inflammation.[25] Accordingly, adenosine triphosphate (ATP) levels were reduced in isolated ileal crypts from TNF$^{\Delta ARE}$ mice, along with increased levels of the MT-UPR marker proteins Hsp60 and (dsRNA-activated protein kinase) Pkr[25] under inflammatory conditions (figure 4A–D). Concomitantly, transcriptional levels of genes involved in signalling pathways related to disturbed mitochondrial function, including MT-UPR (*Trb3*, *Atf5*, *Chop*), antioxidative response (*Hif1a*) and low ATP levels (*Prkaa2*, AMP-kinase) were upregulated in ileal crypts (figure 4E), while expression of *Grp78*, a surrogate marker of ER stress remained unaltered (figure 4F). In line, transmission electron microscopy showed markedly reduced numbers of PCs with typical morphological features at the ileal crypt bases of inflamed TNF$^{\Delta ARE}$ mice. The few remaining Paneth-like cells often exhibited secretory granules with broadened halos, intracytoplasmic vacuolations, dilation of the rough ER, as well as degenerative mitochondrial alterations, including mitochondrial swelling with dissolution and disruption of cristae, loss of matrix density and occasionally formation of intramitochondrial electron-dense inclusions (figure 4G). Autophagy contributes to the mobilisation of cellular energy stores and alterations in autophagy-related proteins have been linked to the disruption of the PC granule exocytosis pathway and degenerating mitochondria.[14] Thus staining for the autophagy marker LC3, an increase in LC3 expression in crypt bases of inflamed TNF$^{\Delta ARE}$ mice was observed accompanying metabolic and morphologic alterations (online supplementary figure 5A,B).

MITOCHONDRIAL IMPAIRMENT IN ISC CAUSES TRANSITION TOWARDS DYSFUNCTIONAL PANETH CELLS

PC and *Lgr5*$^{+}$ ISC alterations concurrent to mitochondrial impairment were present under inflammatory conditions in TNF$^{\Delta ARE}$ mice. Hence, we characterised the role of mitochondrial function on ISC niche appearance using a mouse model in which Hsp60 can be specifically deleted in *Lgr5*$^{+}$ ISC (*Hsp60*$^{flox/flox}$ × *Lgr5*-eGFP-IRES-CreER$^{T2\text{-}Tg}$) via administration of tamoxifen (Hsp60$^{\Delta/\Delta ISC}$).[26] Hsp60 represents a target gene of MT-UPR signalling and constitutes the main chaperone of the mitochondrial matrix.[30] Thus, loss of Hsp60 leads to disturbed proteostasis in mitochondria and subsequent activation of MT-UPR signalling.[26] Consequently, Hsp60 deficiency results in mitochondrial dysfunction, including reduced mitochondrial respiration and a drop in cellular ATP content.[26] Confirming MT-UPR activation on Hsp60 loss, transcription of the cochaperone and surrogate marker of MT-UPR, *Hsp10* increased early after induction of Hsp60 deletion in parallel with induction of *Trb3*, *Chop, Hif1a and Prkaa2* (figure 5A). Following *Lgr5* and Lyz expression in the ileum of Hsp60$^{\Delta/\Delta ISC}$ mice for up to 6 days after the end of tamoxifen treatment, transient changes of the ISC niche were characterised. At day 2, the proportion of highly *Lgr5* expressing crypts dropped (figure 5B,C). Parallel efforts to characterise PC phenotypes demonstrated that *Lgr5*$^{-}$ Lyz^{+} cell numbers decreased, while numbers of *Lgr5*$^{+}$ Lyz^{+} double positive cells increased, starting at day 0 after end of tamoxifen treatment (figure 5B–D). Along with diminished expression of markers for ISCs and PCs, PC granularity and expression of PC-derived AMPs were reduced in response to Hsp60 loss-induced mitochondrial dysfunction in ISCs (figure 5E–G). Reflecting inflamed TNF$^{\Delta ARE}$ mice, LC3 staining in crypt bases of Hsp60$^{\Delta/\Delta ISC}$ mice depict induction of autophagy (online supplementary figure 5C) along with metabolic and morphological alterations of the ISC niche. To exclude the possibility of mitochondrial dysfunction-mediated cell death of *Lgr5*$^{+}$ ISC and Lyz^{+} cells, tissue sections from day 2, when loss of *Lgr5* expression was most pronounced, were costained for TUNEL and eGFP or Lyz, respectively. Furthermore, tissue sections were stained for the apoptosis marker cleaved caspase (CC) 3, confirming absence of enhanced apoptosis at day 2 after the end of tamoxifen treatment, but indicating increased apoptosis in crypt basis at days 4 and 6 (online supplementary figure 6). Hsp60 deficiency in *Lgr5*$^{+}$ ISCs was associated with a complete loss of proliferation as indicated by Ki67 staining (online supplementary figure 7A). However, expression of *Olfm4* and *Hopx*, a marker of +4 reserve stem cells potentially contributing to *Lgr5*$^{+}$ ISC replenishment,[31] was retained and transiently enhanced in crypts (online supplementary figure 7B,C). In line, cells above the crypt basis remained Hsp60 and Ki67 positive throughout the observed time points (online supplementary figure 7A). Crypt-based cells regained Hsp60 and Ki67 expression from day 4 on, indicating apoptotic cell death and extrusion of Hsp60 deficient cells. *Lgr5*$^{+}$ ISC can differentiate into PCs, and vice versa, dedifferentiation of PCs and acquisition of stem-like features has been described following loss of CBC ISCs.[9 10] To determine if dysfunctional PCs arise from mitochondrial function-impaired ISCs, we stained for Lyz and Hsp60. Hsp60 negative cells directly originated from *Lgr5*$^{+}$ ISCs that had suffered from mitochondrial dysfunction. The ratio of Lyz^{+} cells in which Hsp60 could not be detected was increased at day 0 and day 2 (figure 5H,I), indicating *Lgr5*$^{+}$, Hsp60^{-} ISCs to acquire Lyz expression via mechanisms initiated by mitochondrial dysfunction. Furthermore, reduced PC granularity and diffuse Lyz staining was associated with lack of Hsp60 in PCs (figure 5J). In summary, these data suggest that mitochondrial impairment, including reduced mitochondrial respiration, initiates a transition of *Lgr5*$^{+}$ ISCs towards a PC-like phenotype. However, the inability of these *Lgr5*$^{+}$ Lyz^{+} double positive cells to adjust their mitochondrial function to the new cell-phenotypic demand (due to lack of Hsp60), seems to hamper differentiation into functionally mature PCs (figure 5K). Interestingly, costaining

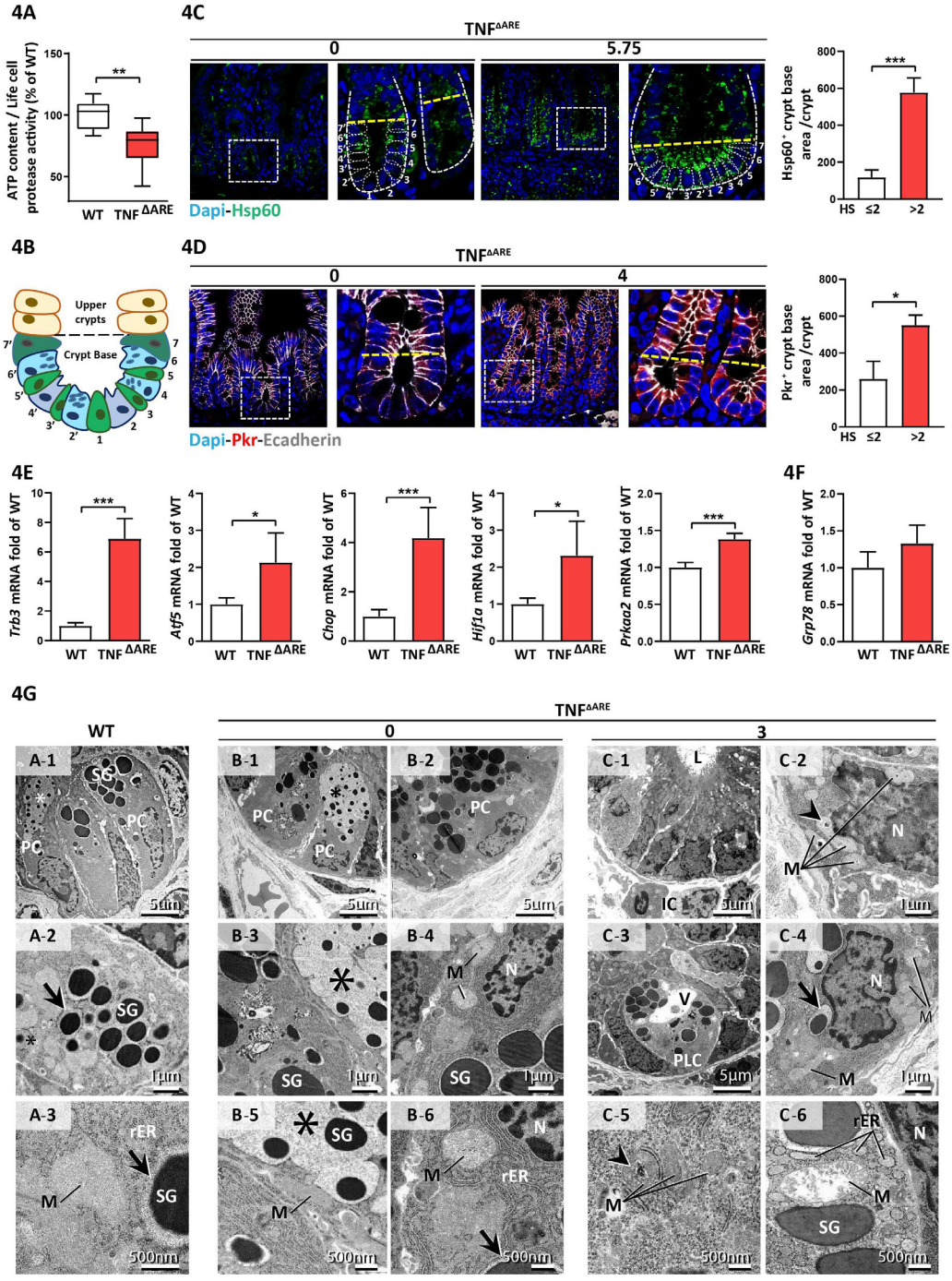

Figure 4 Inflammation in TNF$^{\Delta ARE}$ mice is associated with mitochondrial dysfunction in ileal crypts Isolated ileal crypts and tissue sections from TNF$^{\Delta ARE}$ mice and WT littermates were analysed. (A) ATP content of primary isolated crypts relative to life cell protease activity measured by a fluorescence assay (n=10/7). (B) Overview of crypt structure and illustration of the area used for protein quantification. (C) IF images of Hsp60 (green) counterstained with Dapi (nuclei, blue), including magnifications. Numbers above the pictures indicate the HS of the respective tissue section. Right: corresponding quantification. (D) Costaining of Pkr (green) and E-cadherin (IEC borders, grey) counterstained with Dapi (nuclei, blue), including magnifications. Numbers above the pictures indicate the HS of the respective tissue section. Right: corresponding quantification. (E) qRT-PCR analysis of primary ileal crypts for genes involved in mitochondrial MT-UPR, mitochondrial signalling and (F) ER stress (n=6). Statistics were performed by unpaired *t*-test. Bars represent mean+SEM. Asterisks indicate significant differences *p<0.05, **p<0.01, ***p<0.001. (G) Transmission electron microscopy of ileal crypt bases. Panel *A*: WT; *A1-2*: PCs display abundant, apical, electron-dense SGs with narrow halos (arrow). Asterisks mark secretory granules with small electron dense cores and wide rims of flocculent material of low electron-density. *A-3*. Unaltered appearance of rER and mitochondria (M) in a WT-PLC. *B*: non-inflamed TNF$^{\Delta ARE}$ mice; *B-1–6*: PC ultrastructure essentially resembles WT mice. N: nucleus. *C*: inflamed TNF$^{\Delta ARE}$ mice. *C-1–2*: Few remaining cells with PLC-typical location and morphology often show vacuolation (V) and broadened halos of secretory granules. IC: infiltrating inflammatory cell *C-4–6*: Mitochondrial lesions in PLC include intramitochondrial inclusions (*C-4, C-5*), mitochondrial swelling with dissolution and disruption of cristae, and loss of matrix density and also distension of the rER (*C-6*). ARE,AU-rich (adenosin-uracil) elements; CD, Crohn's disease; HS, histopathological score; IEC, intestinal epithelial cell; PC, Paneth cell; rER, rough endoplasmic reticulum; SG, secretory granule; TNF, tumour necrosis factor; WT, wild type.

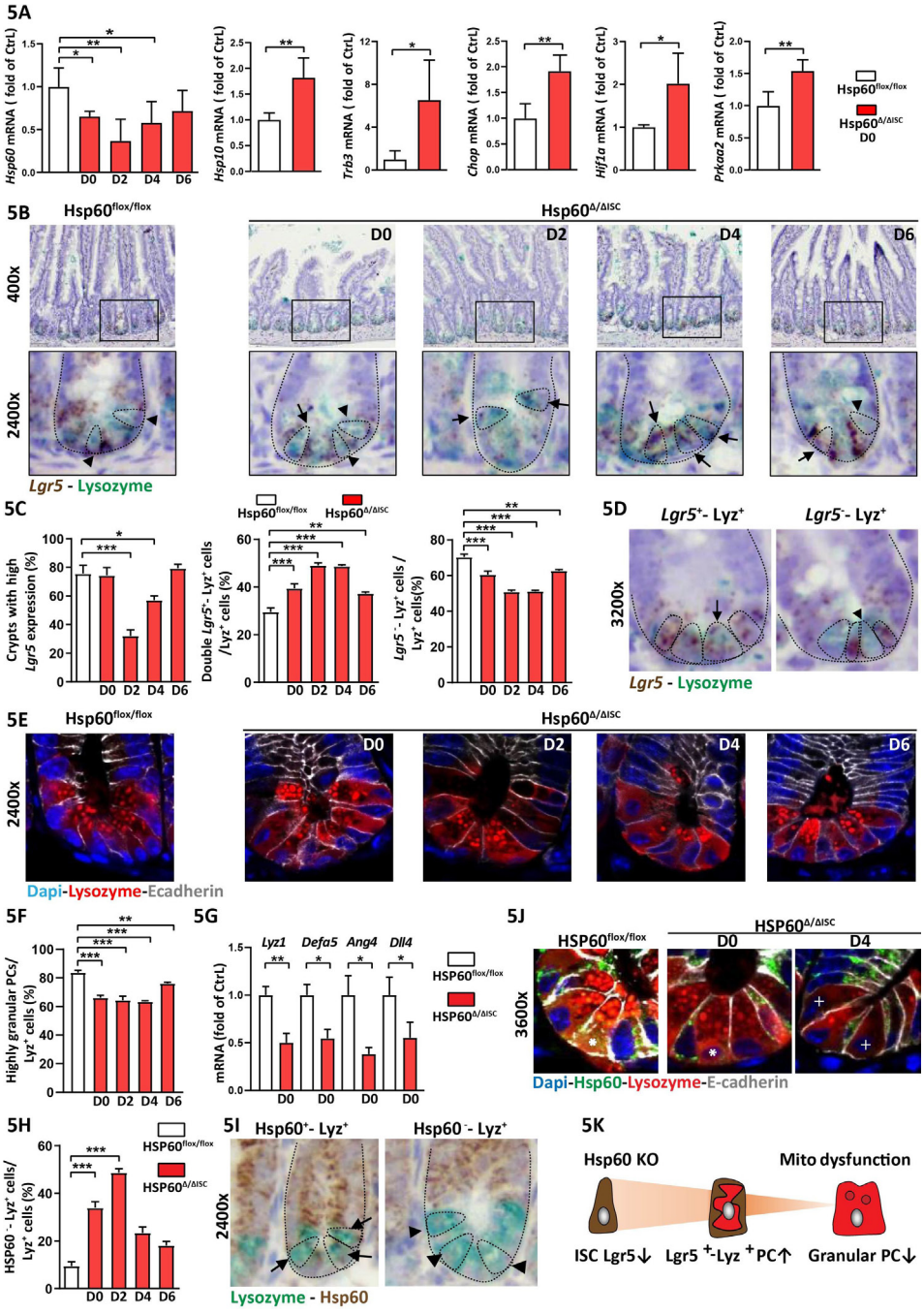

Figure 5 Mitochondrial impairment in ISC causes transition towards dysfunctional Paneth cells Ileal tissue sections and IEC isolates of Hsp60$^{flox/flox}$ mice and Hsp60$^{\Delta/\Delta ISC}$ mice were analysed at different time points after end of tamoxifen treatment. (A) qRT-PCR analysis of IECs for *Hsp60* and genes involved in mitochondrial MT-UPR and mitochondrial signalling at day 0. (B) *Lgr5 in situ* hybridisation (brown) and lysozyme (Lyz, turquoise) immunehistochemistry (IHC) costaining, lower panel: magnifications, dotted lines indicate crypt and cell borders, arrow-heads indicate Lyz$^+$ cells, arrows indicate *Lgr5*—Lyz double-positive cells. (C) Quantification of the proportion of crypts with high *Lgr5* expression (≥10 *Lgr5* transcripts), the proportion of *Lgr5*—Lyz double-positive cells, and the proportion of *Lgr5* negative, Lyz single-positive cells over time. (D) Representative pictures of *Lgr5*—Lyz double-positive cells, and *Lgr5* negative, Lyz single-positive cells; dotted lines indicate crypt and cell borders, arrows indicate *Lgr5*—Lyz double-positive cells, arrow-heads indicate *Lgr5* negative, Lyz single-positive cells. (E) IF costaining of Lyz (red) and E-cadherin (IEC borders, grey) counterstained with Dapi (nuclei, blue) showing granular and non-granular staining pattern. (F) Quantification of the proportion of highly granular Lyz$^+$ cells (≥2 granules). (G) qRT-PCR analysis of IECs from day 0 for PC-derived AMP and *Dll4*. (H) Quantification of the proportion of Hsp60 negative, Lyz single positive cells. (I) Representative pictures of IHC costaining for Hsp60 (brown) and Lyz (turquoise) used for quantification; dotted lines indicate crypt and cell borders, arrow indicates Hsp60—Lyz double positive cells, arrow-heads indicate Hsp60 negative, Lyz single-positive cells. (J) IF costaining of Hsp60 (green), Lyz (red), and E-cadherin (IEC borders, grey) counterstained with Dapi (nuclei, blue), including magnifications. Asterisks indicate Hsp60—Lyz double positive, highly granular Paneth cells, crosses indicate Hsp60 negative, Lyz single-positive cells, depicting a diffuse Lyz staining. (K) Schematic representation of the main findings in this figure. Statistical analyses were performed by one-way ANOVA followed by Tukey test or unpaired *t-test*. Bars represent mean+SEM. Asterisks indicate significant differences *p<0.05, **p<0.01, ***p<0.001. AMP, antimicrobial peptides; ANOVA, analysis of variance; IEC, intestinal epithelial cell; MT-UPR,mitochondrial unfolded protein response;

of Hsp60 with Mucin 2 (Muc2), Chromogranin A (ChgA) or doublecortin-like kinase 1 (dclk1) as markers for the secretory IEC types (goblet cells, enteroendocrine cells and tuft cells, respectively) indicated that ISC suffering from mitochondrial dysfunction only acquired Lyz expression, since Muc2, ChgA and dclk1 expressing cells remained Hsp60 positive (online supplementary figure 8A–C). At day 6 after tamoxifen treatment, ISCs and PCs regained normal phenotypes comparable to *Hsp60*$^{flox/flox}$ mice (figure 5B,C,E,F,H). At this time point, *Hsp60* mRNA expression in IEC returned to control levels (figure 5A). The complete regain of Hsp60^{+}, *Lgr5*$^{+}$ ISCs and a normal ISC niche phenotype indicates replenishment of *Lgr5*$^{+}$ ISCs from reserve ISC populations as described before.[9 32]

CRYPTS FROM INFLAMED TNF$^{\Delta ARE}$ MICE FAIL TO GROW INTO ORGANOIDS

Further investigating the role of mitochondrial function on ISC niche-regulation under inflammatory conditions, primary crypts of non-inflamed and inflamed TNF$^{\Delta ARE}$ mice were isolated and seeded in medium without Wnt factors.[33] Addition of Wnt factors to the medium is not essential for small intestinal (SI) organoid culture and has been linked to the presence of PCs providing these signals naturally.[34] Ileal crypts from inflamed mice displayed reduced *Lgr5* and *Lyz* expression, confirming figure 1 (figure 6A,B). Consistently, ileal crypts from inflamed, but not non-inflamed TNF$^{\Delta ARE}$ mice almost completely failed to grow into organoids. Remaining organoids showed a severe defect in de-novo crypt formation (budding) (figure 6C). In non-inflamed TNF$^{\Delta ARE}$ mice and WT littermates, seeding efficiency and budding were comparable (online supplementary figure 9A), confirming inflammation and not genotype as responsible for impaired growth. Of note, crypts derived from the jejunum, directly adjacent to the inflamed ileum but showing no tissue pathology in TNF$^{\Delta ARE}$ mice, also displayed a reduced ability to form organoids (figure 6D). Applying an intestinal organoid culture medium supplemented with Wnt factors directly after crypt isolation did not rescue growth (online supplementary figure 9B). Hence, it is likely that disturbances of both *Lgr5*$^{+}$ ISCs and PCs contribute to the inflammation-induced growth defect.

MITOCHONDRIAL RESPIRATION IS REQUIRED TO MAINTAIN STEMNESS AND PC FUNCTIONALITY

The metabolism of cells constituting the ISC niche is coordinated to support each other's demand and particularly mitochondrial oxidative phosphorylation (OXPHOS) is fine tuned to meet the requirements of different IEC subtypes.[8 24] Since crypts derived from an inflammatory environment and Hsp60$^{\Delta/\Delta ISC}$ organoids both display mitochondrial dysfunction, ISC niche alterations and a growth defect (figures 4 and 6A–D, online supplementary figure 9C,D), we determined mRNA expression levels of key factors involved in OXPHOS and glycolysis in primary crypt derived from non-inflamed and inflamed TNF$^{\Delta ARE}$ mice.

Pdha, belonging to the pyruvate dehydrogenase complex (PDC), *Yy1*, a transcriptions factor regulating mitochondrial complex I genes and *cytochrome c oxidase (Cox) IV* were consistently reduced (figure 6E). PDC acts as gatekeeper of metabolism by linking cytoplasmic glycolysis to the TCA cycle and OXPHOS, Hence, oligomycin, blocking OXPHOS and dichloroacetate (DCA), targeting PDC to shift ATP generation from glycolysis to OXPHOS[35] (figure 6F), were used to characterise the role of metabolism on ISC niche function. Murine ileal WT organoids and human SI organoids were treated with sublethal doses of oligomycin (online supplementary figure 9E) or DCA. Organoids treated with oligomycin depict lower numbers of Lyz^{+} cells per crypt and reduced PC granularity (figure 6G). Concomitantly, transcriptional levels of *Lgr5*, *Lyz* and *Ang4* were reduced, while *Chop, Hif1a* and *Prkaa* were upregulated (figure 6G). Noteworthy, these results were mirrored in human intestinal organoids (figure 6H). In contrast, DCA had only minimal effects on these readouts (online supplementary figure 10).

REINFORCING MITOCHONDRIAL RESPIRATION RESTORES INFLAMMATION-IMPRINTED DYSFUNCTION OF THE ISC NICHE

Finally, we tested if the inflammation-associated growth defect in TNF$^{\Delta ARE}$ mice-derived crypts could be reversed by DCA. Indeed, addition of DCA to the organoid culture medium directly after seeding rescued the ability of inflamed TNF$^{\Delta ARE}$ mice-derived ileal crypts to grow into organoids and form de-novo crypts (figure 6J). Strikingly, DCA withdrawal subsequent to passaging at day 8 of culture conferred no negative effects to organoid growth compared with continued DCA treatment (figure 6K,L). Comparing DCA-exposed organoids derived from inflamed TNF$^{\Delta ARE}$ mice and WT mice, transcriptional level of ISC and PC-associated genes largely converged (figure 6M). These data demonstrate that activation of OXPOHOS via inhibition of glycolysis is sufficient to restore inflammation-imprinted metabolic dysfunction of the ISC niche.

The persisting regain of stemness after withdrawal of DCA underlines the reversible nature of ISC alterations under inflammatory conditions, making ISC niche metabolism an attractive target for therapeutic interventions (figure 7).

Discussion

IBDs, including CD and ulcerative colitis, constitute a global health problem.[36] A major challenge in the treatment of CD is the heterogeneity of the disease, with only subsets of patients responding to therapies like administration of anti-TNF antibodies.[37] The great number of susceptibility genes identified along with a range of different environmental triggers, might account for these difficulties, implicating diverse mechanisms contributing to the variable phenotypes of CD. Several CD-relevant pathways converge on the level of PCs, like ER stress, autophagy and bacterial recognition and consistently, the presence of NOD2 and ATG16L1 disease-associated alleles as well as bacterial infection have been demonstrated to affect PC phenotype.[12 14 15 38] Hence, aberrant PC phenotypes have been proposed as a biomarker to stratify patients with CD according to similar disease mechanisms in order to yield better treatment outcomes.[13] The data presented here implicate that determining ISC niche appearance improves risk stratification of patients with CD, and that targeting the underlying mitochondrial dysfunction evolves as a novel strategy for therapy.

Reduced PC functionality has been extensively described for CD in the context of AMP production and alterations of the intestinal microbiota.[3 5 15 27] However, PCs serve as multifunctional guardians of the crypt, also providing essential signals for the ISC niche.[27] PCs evolve directly above the crypt base, and *Lgr5*$^{+}$ ISCs compete for available surface of their own direct progeny,[34] implicating ISC changes concomitant to PC abnormalities. Consequently, we found diminished *Lgr5* expression in patients with CD and in inflamed TNF$^{\Delta ARE}$ mice, reflecting the inflammation-associated gradual loss of PC function. Furthermore, in patients with CD, LYZ and *LGR5* showed a distorted

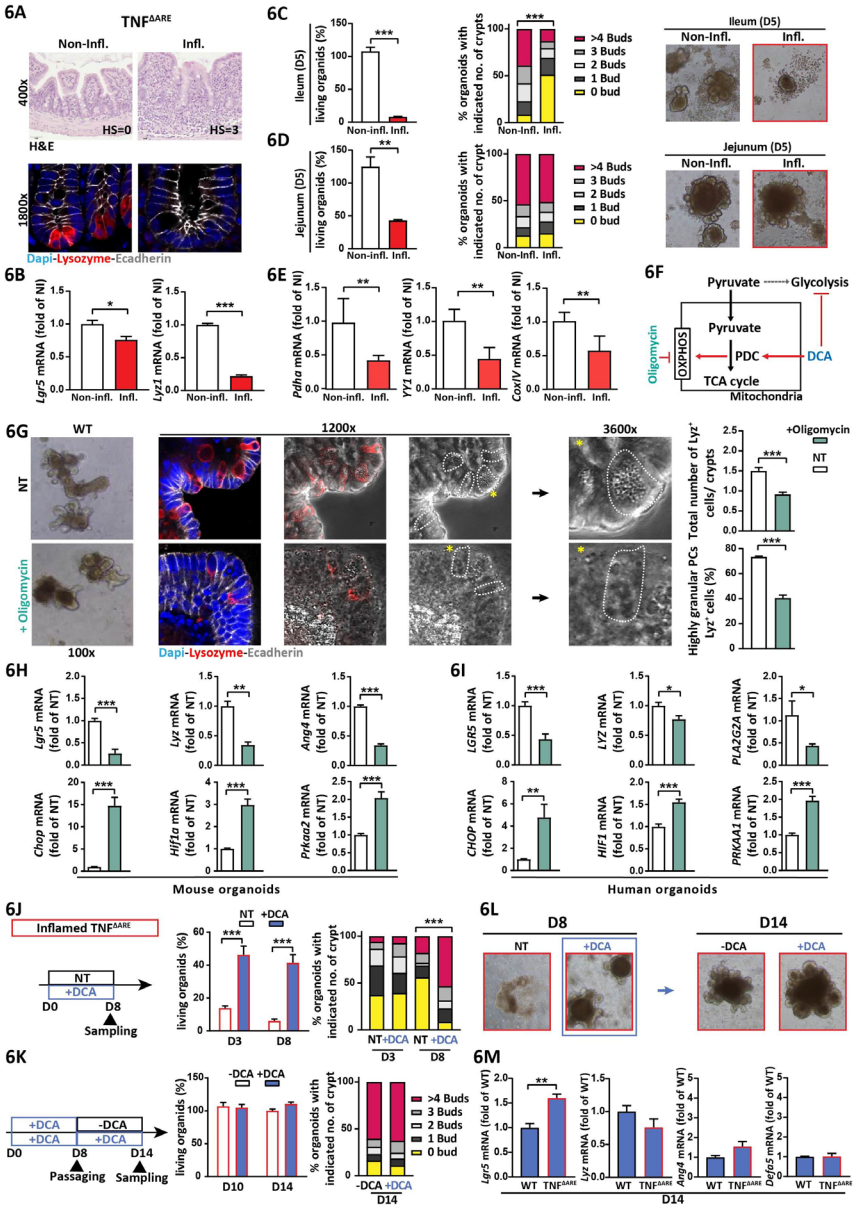

Figure 6 Mitochondrial respiration determines stemness and PC functionality under inflammatory conditions (A–E) Ileal tissues and crypts derived from non-inflamed and inflamed TNF$^{\Delta ARE}$ mice were analysed. (A) Representative pictures of ileal sections; top: H&E staining with histopathological score indicated; bottom: IF costaining of Lyz (red) and E-cadherin (grey) counterstained with Dapi (nuclei, blue) showing absence of PCs in inflamed tissue. (B) qRT-PCR analysis of primary ileal crypts for *Lgr5* and *Lyz* (n=6). (C,D) Characterisation of intestinal organoids derived from ileal (C) and jejunal (D) crypts at day 5 of ex vivo culture. Left: Proportion of living organoids; middle: quantification of de novo crypt formation (budding); right: representative bright field pictures. (E) qRT-PCR analysis of primary ileal crypts for metabolism-determining genes (n=6). (F) Schematic representation of oligomycin and DCA targets. (G,H) Ileal organoids derived from WT mice were treated with oligomycin for 24 hours. (G) Left: bright field and IF costaining of Lyz (red) and E-cadherin (IEC borders, grey) counterstained with Dapi (nuclei, blue). Dotted lines indicate cell borders of Lyz$^+$ cells; asterisks indicate Lyz$^+$ cells magnified in the pictures on the right side. Right: quantification of Lyz$^+$ cell numbers per crypt (upper graph) and the proportion of highly granular (≥2 granules) Lyz$^+$ cells (lower graph). (H) qRT-PCR analysis of intestinal organoids for *Lgr5* and Paneth cell function-associated genes (upper panel) and for genes associated with mitochondrial signalling (lower panel, n=6). (I) Same analysis as in (H) for human organoids derived from the small intestine and treated with oligomycin for 24 hours (n=6). (J–L) Ileal organoids derived from inflamed TNF$^{\Delta ARE}$ mice were analysed (n=6). (J) From left to right: experimental scheme (D0=isolation of primary crypts and start of culture), non-treated and DCA-treated organoids were compared; proportion of living organoids at day 3 and day 8 of culture; quantification of de novo crypt formation at day 3 and day 8. (K) From left to right: experimental scheme, DCA-treated organoid cultures were passaged at day 8, and subsequently cultured in control (-DCA) and DCA-containing medium, respectively, until day 14; proportion of living organoids at day 10 and day 14 of culture; quantification of de novo crypt formation at day 14. (L) Representative bright field pictures of organoids at day 8 (before passaging) and at day 14 of culture. (M) WT and inflamed TNF$^{\Delta ARE}$ mice-derived ileal organoids were treated with DCA for 14 days. qRT-PCR analysis for *Lgr5* and Paneth cell function-associated genes. Statistics were performed by unpaired *t*-test when comparing two groups and by one-way ANOVA followed by Tukey test for three-group comparisons, respectively. Statistics for budding analyses were performed by Kruskal–Wallis test on ranks. Bars represent mean+SEM. Asterisks indicate significant differences *p<0.05, **p<0.01, ***p<0.001. ANOVA, analysis of variance; ARE,AU-rich (adenosin-uracil) elements; DCA, dichloroacetate; Lyz$^+$, Lyz positive; OXPHOS, oxidative phosphorylation; WT, wild type.

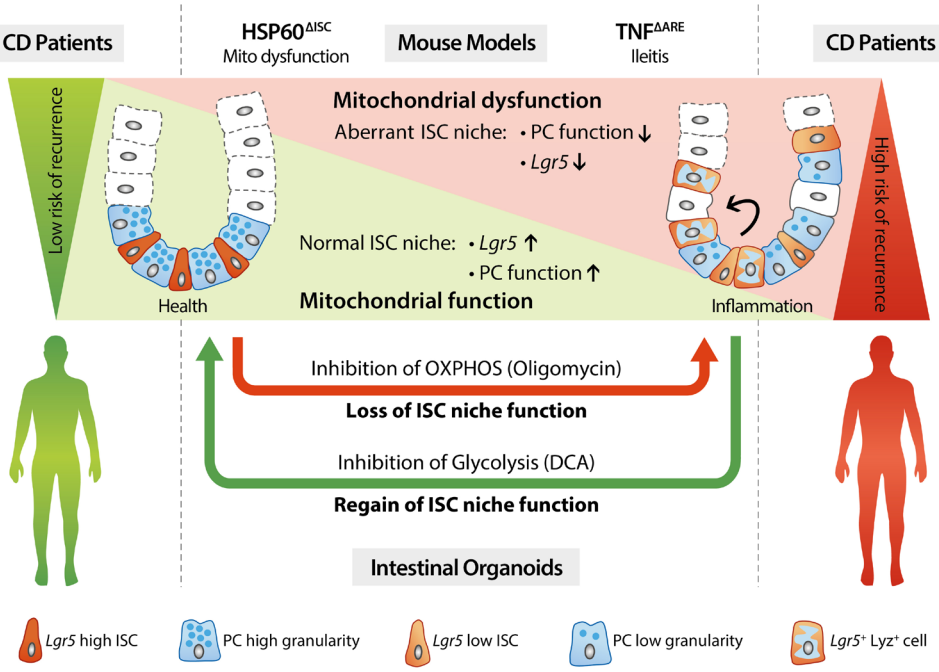

Figure 7 Mitochondrial impairment drives ISC transition towards dysfunctional PCs predicting Crohn's disease recurrence Schematic representation of the main findings of this work. Targeted disruption of mitochondrial function in ISCs leads to transition of ISCs into dysfunctional PCs. Under inflammatory conditions, mitochondrial impairment in the ISC niche results in ISC exhaustion and generation of dysfunctional PCs characterised by loss of Lyz positive granules, concomitant to aberrant *Lgr5* and Lyz expression in upper crypts. These alterations precede tissue pathology and serve as predictive markers for early endoscopic recurrence in CD. Ex vivo, the inhibition of mitochondrial respiration (OXPHOS) in intestinal organoids reflects the impact of an inflammatory environment on the ISC niche, whereas reinforcement of OXPHOS by inhibition of glycolysis is able to override inflammation-imprinted changes of the ISC niche. ARE,AU-rich (adenosin-uracil) elements; CD, Crohn's disease; ISC, intestinal stem cell; Lyz, Lysozyme; OXPHOS, oxidative phosphorylation; PC, Paneth cell; TNF, tumour necrosis factor.

expression pattern with PCs and ISCs abundantly present in upper crypts. So far, *Lgr5*$^+$ ISC loss has been described in the primary response to DSS-induced inflammation and on high-dose γ-irradiation.[9 39] The temporary depletion and rapid restoration of these cells following acute injury seems to underlie the regenerative response of crypts. Under these conditions, PCs contribute to the repair and regeneration of damaged intestinal tissue by acquiring stem like features.[9–11] However, irradiation and DSS-induced inflammation cause acute mucosal injury and do not reflect the chronic inflammatory conditions of IBD pathology. Despite reduced *Lgr5* expression, crypts derived from DSS-treated mice show an enhanced capacity to form organoids,[9] in contrast to crypts from inflamed TNF$^{\Delta ARE}$ mice that fail to give rise to organoids. Hence, the phenotypic changes of the ISC niche under chronic inflammation are likely not associated with healing processes but rather indicate stemness exhaustion as a feature of pathology. Moreover, ISC niche abnormalities were detected before onset of severe tissue pathology in TNF$^{\Delta ARE}$ mice and in non-affected tissue margins of patients with CD, suggesting that these changes most likely represent early, molecular marker of inflammatory changes.

Additionally, we provide experimental evidence for a direct role of mitochondria in the development of dysfunctional PCs using an ISC-specific mouse model of mitochondrial dysfunction and ex vivo inhibition of OXPHOS in organoid cultures. Experimental disturbance of mitochondrial function reduced stemness and PC functionality, demonstrating dysfunctional PCs as direct descendants of ISCs suffering from mitochondrial impairment. Thus, while mitochondrial dysfunction in ISC seems to disturb the balance between self-renewal and differentiation, the inability to fine-tune mitochondrial function subsequently seems to interfere with differentiation processes, impeding normal PC maturation.

This is in line with the pivotal role of mitochondria in ISC fate through regulation of the metabolic switch during differentiation.[24] In *Lgr5*$^+$ ISCs isolated from the mouse small intestine, OXPHOS highly contributes to cellular bioenergetics, and mitochondrial activity further increases with differentiation and de-novo crypt formation in intestinal organoids,[8] indicating why ISC and ISC differentiation processes might be particularly vulnerable to mitochondrial impairment. OXPHOS inhibition and the subsequent decrease in ISC and PC marker genes was associated with transcriptional activation of Chop, hypoxia-inducible factor 1-α and AMP kinase in murine and human intestinal organoids. All of these genes are involved in metabolic regulation and link mitochondrial homeostasis to CD-relevant pathomechanisms including MT-UPR, ROS signalling and energy sensing.[24 40–42]

Most remarkable, ex vivo culture experiments using intestinal crypts derived from inflamed TNF$^{\Delta ARE}$ mice suggest (I) that the inflammatory environment imprints the ISC niche towards reduced stemness and PC function, (II) that these changes persist under normal culture conditions and cannot be overcome by addition of Wnt factors, (III) that a targeted metabolic intervention using DCA treatment rescues stemness and reverses the inflammatory imprinting, allowing organoids to propagate under normal culture conditions. DCA treatment results in diminished glycolysis and improved mitochondrial respiration, an ability used in the therapy of several different solid tumours to reverse the Warburg effect in cancer cells.[35] Identification of target metabolites conferring to ISC niche homeostasis could be a promising target of future research.

The cause of mitochondrial disturbances present in patients with CD and mouse models of intestinal inflammation is currently unknown. In general, enterocytes of patients with IBD have been reported to display swollen mitochondria with irregular cristae indicative of impaired function,[43] and inflammation is associated with hypoxia. Infiltrating immune cells, invading pathogens and the increased energy demand of resident cells limit the available oxygen,[44] and together with reduced blood supply,[45] these changes contribute to the hypoxic conditions under chronic inflammation. Furthermore, polymorphisms in genes impacting mitochondrial functions, mitochondrial carrier protein *uncoupling protein* (*UCP*) *2* and *SLC22A5*, encoding the carnitine transporter OCTN2, have been described as risk factors in IBD.[46 47] UCP2 is proposed to control the speed of the TCA cycle, and production of mitochondrial ROS, and to promote the metabolic shift from glucose to fatty acid oxidation.[48] OCTN2 transports long-chain fatty acids conjugated to carnitine into mitochondria for β-oxidation. β-oxidation is particularly implicated in CD pathogenesis, and consequently, pharmacological inhibition of intestinal fatty acid β-oxidation as well as genetic ablation of OCTN2 results in experimental colitis.[49 50] These genetic risk factors might act in concert with other CD-relevant pathways described above and might render IECs particularly sensitive to environmental triggers of inflammation.

In patients with CD, the proportion of PCs with aberrant granule structure and diffuse LYZ distribution has been shown to correlate with the cumulative number of *NOD2* and *ATG16L1* risk alleles,[13] linking multiple CD genetic susceptibility loci to a defined PC phenotype. High proportions of abnormal PCs were associated with shorter time to disease recurrence after surgery in patients with a more aggressive clinical disease course.[13] Our findings on PC granularity corroborate these findings in an independent patient cohort refining the endpoint of prediction to early postoperative lesions observed by ileocolonoscopy 6–12 months after surgery, and expand the set of predictive cellular markers to *Lgr5*$^{+}$ ISC and to the location of expression. Abnormal PC morphology has also been linked to an activated immune response gene signature in crypts from patients with CD[13] and to a transcriptional profile of cytokine stimulation in mice with hypomorphic expression of Atg16l1.[14] Together with the evidence presented here, this suggests an interrelated role of molecular inflammation and metabolism for ISC and PC phenotype. Furthermore, our data indicate some kind of signal propagation from adjacent, inflamed tissue regions, as jejunal organoids derived from inflamed TNF$^{\Delta ARE}$ mice display impaired growth.

In conclusion, we identified ISC niche alterations as target of molecular inflammatory changes and predictive marker of early endoscopic recurrence in CD. In this context, we demonstrated that impaired mitochondrial function is linked to CD-associated loss of stemness and the generation of dysfunctional PC phenotypes. Mitochondria-derived signals might collaborate with IBD susceptibility genes to impact on ISC niche functionality, and in concert with environmental factors, such as intestinal microbiota or diet, contribute to the loss of ISC niche homeostasis observed in ileal CD. By implementing a drug-related shift towards mitochondrial respiration, we provide a proof-of-concept for the importance of mitochondrial metabolism in regulating ISC and PC functions and thereby rationalise a novel treatment approach for CD.

Author affiliations
[1]Chair of Nutrition and Immunology, Technische Universität München, Freising-Weihenstephan, Germany
[2]Department of Gastroenterology, Hôpital Saint-Louis, APHP, INSERM U1160, Université de Paris 1, Paris, Île-de-France, France
[3]Research Unit Analytical Pathology, Helmholtz Zentrum München, Neuherberg, Germany
[4]Chair of Nutrition Physiology, Technische Universität München, Freising-Weihenstephan, Germany
[5]ZIEL Institute for Food & Health, Technische Universität München, München, Germany

Contributors SK, ER and DH designed the experiments, performed data analysis and wrote the manuscript. SK, ER and EB performed mouse and organoid culture experiments. SK performed tissue analysis of patients. AB performed the transmission electron microscopy. EG, NW, AM and PG supported analyses. MA and NH provided patient samples.

Funding DH received funding by the Deutsche Forschungsgemeinschaft (DFG, German Research Foundation) SFB 1371 (Projektnummer 395357507; P01) and Priority Programme SPP 1656. DH and MA received funding from the Helmsley Cheritable Trust (IBDOT).

Competing interests None declared.

Patient consent for publication Not required.

Provenance and peer review Not commissioned; externally peer reviewed.

Data availability statement All data relevant to the study are included in the article or uploaded as supplementary information. Additional data are available on request.

ORCID iDs
Eva Rath http://orcid.org/0000-0003-1910-1162
Matthieu Allez http://orcid.org/0000-0002-2012-7522
Dirk Haller http://orcid.org/0000-0002-6977-4085

REFERENCES

1 Maloy KJ, Powrie F. Intestinal homeostasis and its breakdown in inflammatory bowel disease. *Nature* 2011;474:298–306.
2 Fritz T, Niederreiter L, Adolph T, *et al*. Crohn's disease: NOD2, autophagy and ER stress converge. *Gut* 2011;60:1580–8.
3 Jäger S, Stange EF, Wehkamp J. Inflammatory bowel disease: an impaired barrier disease. *Langenbecks Arch Surg* 2013;398:1–12.
4 Salzman NH, Ghosh D, Huttner KM, *et al*. Protection against enteric salmonellosis in transgenic mice expressing a human intestinal defensin. *Nature* 2003;422:522–6.
5 Salzman NH, Hung K, Haribhai D, *et al*. Enteric defensins are essential regulators of intestinal microbial ecology. *Nat Immunol* 2010;11:76–82.
6 Andersson-Rolf A, Zilbauer M, Koo B-K, *et al*. Stem cells in repair of gastrointestinal epithelia. *Physiology* 2017;32:278–89.
7 Yilmaz Ömer H., Katajisto P, Lamming DW, *et al*. mTORC1 in the Paneth cell niche couples intestinal stem-cell function to calorie intake. *Nature* 2012;486:490–5.
8 Rodríguez-Colman MJ, Schewe M, Meerlo M, *et al*. Interplay between metabolic identities in the intestinal crypt supports stem cell function. *Nature* 2017;543:424–7.
9 Schmitt M, Schewe M, Sacchetti A, *et al*. Paneth cells respond to inflammation and contribute to tissue regeneration by acquiring stem-like features through SCF/c-Kit signaling. *Cell Rep* 2018;24:2312–28.
10 Roth S, Franken P, Sacchetti A, *et al*. Paneth cells in intestinal homeostasis and tissue injury. *PLoS One* 2012;7:e38965.
11 Yu S, Tong K, Zhao Y, *et al*. Paneth cell multipotency induced by Notch activation following injury. *Cell Stem Cell* 2018;23:46–59.
12 Kaser A, Lee A-H, Franke A, *et al*. XBP1 links ER stress to intestinal inflammation and confers genetic risk for human inflammatory bowel disease. *Cell* 2008;134:743–56.
13 VanDussen KL, Liu T-C, Li D, *et al*. Genetic variants synthesize to produce Paneth cell phenotypes that define subtypes of Crohn's disease. *Gastroenterology* 2014;146:200–9.
14 Cadwell K, Liu JY, Brown SL, *et al*. A key role for autophagy and the autophagy gene Atg16l1 in mouse and human intestinal Paneth cells. *Nature* 2008;456:259–63.
15 Adolph TE, Tomczak MF, Niederreiter L, *et al*. Paneth cells as a site of origin for intestinal inflammation. *Nature* 2013;503:272–6.
16 Koslowski MJ, Kübler I, Chamaillard M, *et al*. Genetic variants of Wnt transcription factor TCF-4 (TCF7L2) putative promoter region are associated with small intestinal Crohn's disease. *PLoS One* 2009;4:e4496.
17 Günther C, Martini E, Wittkopf N, *et al*. Caspase-8 regulates TNF-α-induced epithelial necroptosis and terminal ileitis. *Nature* 2011;477:335–9.

18 Garabedian EM, Roberts LJJ, McNevin MS, *et al*. Examining the role of Paneth cells in the small intestine by lineage ablation in transgenic mice. *J Biol Chem* 1997;272:23729–40.
19 Durand A, Donahue B, Peignon G, *et al*. Functional intestinal stem cells after Paneth cell ablation induced by the loss of transcription factor Math1 (Atoh1). *Proc Natl Acad Sci U S A* 2012;109:8965–70.
20 Schaubeck M, Clavel T, Calasan J, *et al*. Dysbiotic gut microbiota causes transmissible Crohn's disease-like ileitis independent of failure in antimicrobial defence. *Gut* 2016;65:225–37.
21 Rath E, Haller D. Mitochondria at the interface between danger signaling and metabolism: role of unfolded protein responses in chronic inflammation. *Inflamm Bowel Dis* 2012;18:1364–77.
22 Beltrán B, Nos P, Dasí F, *et al*. Mitochondrial dysfunction, persistent oxidative damage, and catalase inhibition in immune cells of naïve and treated Crohn's disease. *Inflamm Bowel Dis* 2010;16:76–86.
23 Fukushima K, Fiocchi C. Paradoxical decrease of mitochondrial DNA deletions in epithelial cells of active ulcerative colitis patients. *Am J Physiol Gastrointest Liver Physiol* 2004;286:G804–13.
24 Rath E, Moschetta A, Haller D. Mitochondrial function - gatekeeper of intestinal epithelial cell homeostasis. *Nat Rev Gastroenterol Hepatol* 2018;15:497–516.
25 Rath E, Berger E, Messlik A, *et al*. Induction of dsRNA-activated protein kinase links mitochondrial unfolded protein response to the pathogenesis of intestinal inflammation. *Gut* 2012;61:1269–78.
26 Berger E, Rath E, Yuan D, *et al*. Mitochondrial function controls intestinal epithelial stemness and proliferation. *Nat Commun* 2016;7:13171.
27 Gassler N. Paneth cells in intestinal physiology and pathophysiology. *World J Gastrointest Pathophysiol* 2017;8:150–60.
28 Auzolle C, Nancey S, Tran-Minh M-L, *et al*. Male gender, active smoking and previous intestinal resection are risk factors for post-operative endoscopic recurrence in Crohn's disease: results from a prospective cohort study. *Aliment Pharmacol Ther* 2018;48:924–32.
29 Gionchetti P, Dignass A, Danese S, *et al*. 3rd European Evidence-based Consensus on the Diagnosis and Management of Crohn's Disease 2016: Part 2: Surgical Management and Special Situations. *J Crohns Colitis* 2017;11:135–49.
30 Zhao Q, Wang J, Levichkin IV SS. A mitochondrial specific stress response in mammalian cells. *EMBO J* 2002;21:4411–9.
31 Takeda N, Jain R, LeBoeuf MR, *et al*. Interconversion between intestinal stem cell populations in distinct niches. *Science* 2011;334:1420–4.
32 Tian H, Biehs B, Warming S, *et al*. A reserve stem cell population in small intestine renders LGR5-positive cells dispensable. *Nature* 2011;478:255–9.
33 Zietek T, Rath E. Chapter 3 - Intestinal organoids: Mini-guts grown in the laboratory. In: Davies JA, Lawrence ML, eds. *Organs and organoids*. Academic Press, 2018: 43–71.
34 Sato T, van Es JH, Snippert HJ, *et al*. Paneth cells constitute the niche for LGR5 stem cells in intestinal crypts. *Nature* 2011;469:415–8.
35 Kankotia S, Stacpoole PW. Dichloroacetate and cancer: new home for an orphan drug? *Biochim Biophys Acta* 2014;1846:617–29.
36 Ng SC, Shi HY, Hamidi N, *et al*. Worldwide incidence and prevalence of inflammatory bowel disease in the 21st century: a systematic review of population-based studies. *Lancet* 2018;390:2769–78.
37 Danese S. New therapies for inflammatory bowel disease: from the bench to the bedside. *Gut* 2012;61:918–32.
38 Bel S, Pendse M, Wang Y, *et al*. Paneth cells secrete lysozyme via secretory autophagy during bacterial infection of the intestine. *Science* 2017;357:1047–52.
39 Yan KS, Chia LA, Li X, *et al*. The intestinal stem cell markers BMI1 and LGR5 identify two functionally distinct populations. *Proc Natl Acad Sci U S A* 2012;109:466–71.
40 Giatromanolaki A*et al*. Hypoxia inducible factor 1 and 2 overexpression in inflammatory bowel disease. *J Clin Pathol* 2003;56:209–13.
41 Donohoe DR, Garge N, Zhang X, *et al*. The microbiome and butyrate regulate energy metabolism and autophagy in the mammalian colon. *Cell Metab* 2011;13:517–26.
42 Waldschmitt N, Berger E, Rath E, *et al*. C/EBP homologous protein inhibits tissue repair in response to gut injury and is inversely regulated with chronic inflammation. *Mucosal Immunol* 2014;7:1452–66.
43 Soderholm JD*et al*. Augmented increase in tight junction permeability by luminal stimuli in the non-inflamed ileum of Crohn's disease. *Gut* 2002;50:307–13.
44 Colgan SP, Taylor CT. Hypoxia: an alarm signal during intestinal inflammation. *Nat Rev Gastroenterol Hepatol* 2010;7:281–7.
45 Colgan SP, Curtis VF, Campbell EL. The inflammatory tissue microenvironment in IBD. *Inflamm Bowel Dis* 2013;19:2238–44.
46 Yu X, Wieczorek S, Franke A, *et al*. Association of UCP2 −866 G/A polymorphism with chronic inflammatory diseases. *Genes Immun* 2009;10:601–5.
47 Barrett JC, Hansoul S, Nicolae DL, *et al*. Genome-Wide association defines more than 30 distinct susceptibility loci for Crohn's disease. *Nat Genet* 2008;40:955–62.
48 Pecqueur C, Bui T, Gelly C, *et al*. Uncoupling protein-2 controls proliferation by promoting fatty acid oxidation and limiting glycolysis-derived pyruvate utilization. *FASEB J* 2008;22:9–18.
49 Shekhawat PS, Srinivas SR, Matern D, *et al*. Spontaneous development of intestinal and colonic atrophy and inflammation in the carnitine-deficient JVS (OCTN2−/−) mice. *Mol Genet Metab* 2007;92:315–24.
50 Roediger WE, Nance S. Metabolic induction of experimental ulcerative colitis by inhibition of fatty acid oxidation. *Br J Exp Pathol* 1986;67:773–82.

SUPPLEMENTARY MATERIALS

Khaloian S, *et al. Gut* 2020;0:1–13. doi: 10.1136/gutjnl-2019-319514

Supplementary methods

Ethics statement

The maintenance and breeding of mouse lines and all experiments were approved by the Committee on Animal Health and Care of the local government body of the state of Upper Bavaria (Regierung von Oberbayern; TVA 55.2-1-54-2532-214-2013 and TVA 55.2-1-54-2532-217-2014) and performed in strict compliance with the EEC recommendations for the care and use of Lab. Anim. (European Communities Council Directive of 24 November 1986 (86/609/EEC)). The use of surgically resected CD patient samples was approved by AFFSAPS (IDRCB: 2009-A00205-52), the French Ethic Committee- Hôpital Saint-Louis (CPP 2009/17) and declared to clinicaltrials.gov (NCT03458195). All patients provided an informed written consent. For generation of human organoids, the use of surgically resected human tissue samples was approved by the Ethics Committee of the Medical Faculty of TUM and obtained after prior informed written consent.

Animals

Hsp60$^{flox/flox}$ mice and *Hsp60*$^{flox/flox}$ x *Lgr5*CreER^{T2}-IRES-*Egfp*^{Tg} mice (to generate ISC-specific Hsp60 knockout mice via tamoxifen-induction (*Hsp60*$^{\Delta/\Delta ISC}$ mice) were generated as described previously [1]. TNF$^{\Delta ARE}$ mice were initially provided from Case Western University, Cleveland. All mice were housed (12h light/ dark cycles, 24-26˚C) under SPF conditions and bred for several generations in the animal facility to harmonize the intestinal microbiota. Mice received a standard diet (autoclaved V1124-300; Ssniff, Soest, Germany) and autoclaved water ad libitum. Animals were killed by CO_2 inhalation. TNF$^{\Delta ARE}$ mice and WT littermates were sacrificed at 18 weeks of age.

Induction of postnatal recombination and monitoring of mice

Phytoestrogen free pellets (ssniff, Soest, Germany) were fed for 4 weeks to male 6 weeks old *Hsp60*$^{flox/flox}$ *X Lgr5CreER*^{T2} *Egfp*^{Tg} and their appropriate control mice, respectively. Afterwards, they received 400 mg tamoxifen citrate (Tam) per kg chow feed (LASvendi, Soest, Germany) in pellets *ad libitum* for 7 days. Body weight was monitored before, during and after oral administration of tamoxifen. Body weight, general condition, behavior and intestinal symptoms were assessed by a score

Khaloian S, *et al. Gut* 2020;0:1–13. doi: 10.1136/gutjnl-2019-319514

between 0 and 10 each according to the approved application for animal experiments. Animals were sacrificed at the indicated time points.

Mouse Tissue processing and histopathological analysis

The intestine was removed immediately after killing, trimmed free of adjacent tissue and cleaned of stool. Small intestinal tissues were either immediately fixed for preparation of cross sections or cut open and prepared as a 'swiss role'. Tissues were fixed in 4% PBS buffered formaldehyde, dehydrated and embedded in paraffin (FFPE). For histopathological assessment, 5 µm sections were stained with hematoxylin (of Mayer) and 0.2% eosin (ethanolic solution; both Medite, Burgdorf, Germany) in an automated staining machine (Leica, Soest, Germany). Ileal sections were blindly assessed for mononuclear cell infiltration into lamina propria, crypt hyperplasia, goblet cell depletion and ulcer formation resulting in a score from 0 (not inflamed) to 12 (highly inflamed) as described previously [4].

Transmission electron microscopy (TEM)

For TEM analysis, longitudinal sections of freshly dissected ileum samples were fixed in 2.5% electron microscopy grade glutaraldehyde in 0.1 M sodium cacodylate buffer pH 7.4 (Science Services, Munich, Germany), postfixed in 2% aqueous osmium tetraoxide (Dalton, 1955), dehydrated in gradual ethanol (30–100%) and propylene oxide, embedded in Epon (Merck, Darmstadt, Germany) and cured for 24 hours at 60°C. Semithin sections were cut and stained with toluidine blue. Ultrathin sections of 50 nm were mounted on 200 mesh copper grids, contrasted with uranyl acetate and lead citrate before examination by transmission electron microscopy (Zeiss Libra 120 Plus, Carl Zeiss NTS GmbH, Oberkochen, Germany). Pictures were acquired at 1260-12500x magnification, using a Slow Scan CCD-camera and iTEM software (Olympus Soft Imaging Solutions, Münster, Germany).

Samples from Crohn's disease patients

CD patients' tissue samples were collected during a prospective multicenter study performed by the REMIND group published previously [5]. From this cohort, 70 patients with a paraffin-embedded ileal margin sample available for histological analysis were selected [6]. Patients' characteristics at time of surgery are given in **Supplementary table 1**. Briefly, to assess inflammation at time of surgery, full-thickness 3-µm sections

Khaloian S, *et al. Gut* 2020;0:1–13. doi: 10.1136/gutjnl-2019-319514

of paraffin-embedded ileal margin were stained with hematein eosin saffron (HES). Each section was jointly analyzed by two expert pathologists blinded to the baseline detailed clinical data and to the post-operative outcomes of the patients. The ileal margin was considered as inflamed if (i) mucosal erosion or ulceration or (ii) cryptic abscess/cryptitis was noticed. Ileocolonoscopy was performed 6 -12 months after surgery. The physician performing the endoscopy evaluated the Rutgeerts score. Two physicians checked the colonoscopy's report blinded to histological analysis and post-operative treatment. Endoscopic recurrence was defined as a Rutgeerts score ≥ i2.

Staining procedures

Immunohistochemical (IHC) and immunofluorescence (IF) stainings were performed on 4 µm FFPE tissue sections as described previously [1]. To stain intestinal organoids, Matrigel containing organoids was gently dissolved in cold PBS (Sigma-Aldrich, Taufkirchen, Germany), centrifuged for 5 min at 300 g, and pelleted organoids were carefully fixed in 4% formaldehyde. The suspension was transferred to a microscope glass slide, incubated for 15 min at room temperature and washed subsequently before starting the described [1] staining procedure by adding blocking buffer. Antibodies and dilutions are given in **Supplementary Table 2 and 3**. For detection of apoptosis in FFPE tissue sections (TUNEL-assay) the Apo-BrdU *In Situ* Fragmentation Assay Kit (BioVision, Milpitas, CA) was used according to the manufacturer's instructions. Tissue sections treated with DNaseI (Macherey-Nagel, Düren, Germany) for 15 min immediately after antigen retrieval served as positive controls for the TUNEL assay, murine intestinal segments incubated *ex vivo* in 1 µM staurosporine for 2 h at 37 °C before embedding served as positive controls for CC3 staining. For IF, stainings were visualized using the Flouview FV10i microscope (Olympus, Shinjuku, Japan). For IHC co-staining, sections were incubated for 20 min with 3% H_2O_2 (Sigma- Aldrich, Taufkirchen, Germany) after the first antigen detection using the DAB enhanced liquid substrate system (Sigma-Aldrich). Subsequently, sections were blocked and a second antibody was applied as described above. To detect the second antigen, the HRP green solution set (42 Life sciences GmbH, Bremerhaven, Germany) was used. IHC stainings were scanned and further analyzed using a PreciPoint M8 microscope (Precipoint, Freising, Germany).

In situ hybridization

In situ hybridization for murine *Lgr5,* human *LGR5* and *Olfm4* was performed on 5µm thick tissue sections using the RNAscope-2.5 HD *in situ* assay kit-Brown (ACD, Bio-Techne GmbH, Wiesbaden, Germany) according the manufacturer's instructions. Probes were :RNAscope Probe-Mm-Lgr5; RNAscope Probe-Mm-*Olfm4*; RNAscope Probe-Mm-*Hopx,* and RNAscope Probe-Hs-*LGR5*, all from ACD. Sections were counterstained with hematoxylin, dipped in 0.02% ammonium hydroxide solution and were mounted with xylene based mounting medium. For IHC co-staining, tissue sections were incubated with 3% H_2O_2 (Sigma-Aldrich) for 20 min after conducting *in situ* hybridization stained as described above. For detection of IHC-stained antigens the HRP green solution set (42 Life sciences GmbH, Bremerhaven, Germany) was used. Sections were counterstained with hematoxylin and mounted with xylene based mounting medium. Stained slides were scanned and further analyzed via the PreciPoint M8 microscope.

Quantification of Lysozyme and Lgr5 positive cells

Numbers of Lysozyme (Lyz/LYZ) positive and *Lgr5/LGR5* positive cells were determined in ileal tissue sections stained for Lyz/LYZ by IF and for *Lgr5/LGR5* by *in situ* hybridization. A total number of 80 (for human) or 50 (for mice) well oriented crypts were quantified. Signals arising from cells below the +7 position (<+7) were considered to be located in lower crypt, upper crypt was defined as >+7 (**Supplemental Fig.4A**). To assess *Lgr5/LGR5* expression, dots representing *Lgr5/LGR5* transcripts were counted and crypts containing ≥15 transcripts (for human) and ≥10 transcripts (for mice), respectively, were considered as crypts with high *Lgr5* expression. To assess the granularity of Lyz/LYZ positive cells, a minimum of 150 PCs (ranges between 150 and 334 PCs) were quantified in human tissue sections, for mice all PCs contained in 50 crypts were analyzed. Lyz/LYZ positive cells were considered as highly granular if ≥2 Lyz/LYZ positive granules were visible within the cell. The quantification was performed in a blinded manner.

Quantification of Olfm4 and HopX expression

Quantification of *Olfm4* and *Hopx* expression was performed in small intestinal tissue sections stained by *in situ* hybridization. For $TNF^{\Delta ARE}$ mice, a total number of 50 well oriented ileal crypts were quantified. Total numbers of *Olfm4* positive cells were

Khaloian S, *et al. Gut* 2020;0:1–13. doi: 10.1136/gutjnl-2019-319514

determined in the crypt base (<+7 cells, Supplemental Fig. 4A). For *Hsp60*$^{\Delta/\Delta ISC}$ mice, images of *Hopx in situ* hybridization stainings were analyzed using the ImageJ software. In at least 30 open, well-oriented crypts total crypt IEC area up to the crypt-villus junction was defined and within this area, the area positive for the respective staining was determined. For *Olfm4*, owing to the discontinuous expression pattern of this marker gene, the distance of the most upper *Olfm4* positive cell to the crypt ground (position 0) was measured and normalized to crypt length. All quantifications were performed in a blinded manner.

Quantification of Hsp60 expression

Volocity 2D-3D imaging software was used for the quantification of fluorescence intensity in IF stained tissue section. Quantification of the Hsp60 signals was performed in a minimum of 30 well oriented intestinal crypts. The crypt base area was selected according to **Supplemental Fig. 4A** (<+7 cells) and the positive signal was quantified based on the best fitting threshold, covering positive areas of the crypt base. The same threshold was used for quantification of all sections.

Isolation of primary IECs

Primary IEC were purified as previously described [1]. Approximately 6 cm of intestine were inverted on a needle, vortexed vigorously and incubated (37 °C, 15 min) in DMEM containing 10% fetal calf serum (FCS superior, Biochrom, Berlin), 1.0% Glutamine, 0.8% antibiotics/antimycotics (all Sigma-Aldrich, St Louis, MO) supplemented with 1 mM dithiothreitol (Roth, Karlsruhe, Germany). The IEC suspensions were centrifuged (7 min, 300*g*, RT) and cell pellets were re-suspended in DMEM containing fetal calf serum, L-glutamine and antibiotics. The remaining tissue was incubated in 20 ml PBS (10 min, 37 °C) containing 1.5 mM EDTA (Roth). Thereafter, the tissue was discarded and the cell suspension from this step was centrifuged as mentioned above. Finally, primary IEC were purified by centrifugation through a 20%/40% discontinuous Percoll gradient (GE Healthcare, Uppsala, Sweden) at 600*g* for 30 min.

Primary crypt isolation and intestinal organoid culture

Primary small intestinal crypts from mouse (ileum, jejunum) and human (ileum) were isolated by tissue incubation in 2mM EDTA (Fisher, Dreieich, Germany) and cultured as described elsewhere [1, 7]. Briefly, crypts were embedded in 25µl matrigel (BD

Biosciences, Franklin Lakes, NJ) and cultured in 48 well plates. Until otherwise indicated, murine organoids were grown in crypt culture medium (CCM), advanced DMEM/F12 medium (Gibbco, Cincinnati, OH) containing 2 mM GlutaMax (Gibbco), 10 mM HEPES, penicillin, streptomycin and amphotericin (all Sigma- Aldrich, Taufkirchen, Germany) supplemented with N2, B27 (both Gibbco), 1 mM N-acetylcystein (Sigma- Aldrich), 50 ng ml−1 EGF (ImmunoTools, Friesoythe, Germany), 100 ng ml−1 noggin and 0.5 µg ml−1 R-spondin 1 (both PeproTec, Rocky Hill, NJ). Medium containing Wnt factors suitable for murine organoids (Intesticult) was obtained from STEMCELL Technologies, Grenoble, France. Human organoids were kindly provided by Tamara Zietek and maintained in Human Intesticult medium (STEMCELL Technologies, Grenoble, France). Two days prior to the start of experiments, medium of human organoids was changed to CCM. To assess seeding efficiency, total numbers of propagating organoids were counted at day 1 after seeding (baseline) and numbers of viable organoids were subsequently determined at the indicated time points in the same cell culture plate wells. Data are presented as proportion of living organoids over baseline counts. For quantification of *de novo* crypt formation (budding), organoids were classified according to number of visible bud structures (0, 1, 2, 3, >4). A minimum of 80 organoids (ranging between 80-140) was included in the analyses. *Ex vivo* induction of the *Hsp60* knockout was achieved by adding 1.5 µl of 100 µM (Z)-4-hydroxytamoxifen (4-OHT; LKT, St Paul, MN) to 300 µl CCM per well of a 48 well plate. When indicated, 2.5µM oligomycin (Sigma- Aldrich, Taufkirchen, Germany) or 15mM DCA (Sigma- Aldrich, Taufkirchen, Germany) were added to the culture medium for 24h. Growth measurements were performed using an Olympus CK X 41 microscope and Olympus cellSens Entry software.

Measurement of living cells and cellular ATP content

Life- and dead- cell protease activity was measured using the MultiTox-Fluor Cytotoxicity Assay and ATP content was measured using the CellTiter-Glo Luminescent Cell Viability Assay (both from Promega, Mannheim, Germany), according to the manufacturer's instructions in a 96-well format. Fluorescence and luminescence were measured using the Tecan infinite M200 (Tecan Group Ltd., Männedorf, Switzerland) and the i-control™ Microplate Reader software (Tecan, Grödig, Austria).

Khaloian S, *et al. Gut* 2020;0:1–13. doi: 10.1136/gutjnl-2019-319514

mRNA isolation and quantitative real-time PCR

RNA of a total ileal tissue, ileal IECs, primary crypts and small intestinal organoids was isolated using the NucleoSpin RNAII kit (Macherey-Nagel, Düren, Germany) according to the manufacturer's instructions. Quantitative Real-time PCR (qRT–PCR) was performed using 1 µl cDNA in a Light Cycler 480 system (Roche Diagnostics, Mannheim, Germany) applying the Universal Probe Library system according to the manufacturer's instructions. Primer sequences and probes are given in **Supplementary table 4**. Relative induction of gene mRNA expression was calculated based on Ct values using the expression of *Hprt* for normalization. Data were expressed as fold change over controls.

Statistical analysis

Data of 3–6 animals per experimental group are indicated. Statistical computations were performed using GraphPad Prism (GraphPad, La Jolla, CA). Statistical test used were: unpaired t-test for two group-comparisons or One-Way analysis of variances followed by Tukey test for comparisons comprising more than two groups. To determine statistically significant differences in *de novo* crypt formation, a Kruskal–Wallis test on ranks followed by Dunnś test was performed. Correlation analyses were performed according to Pearson test. Fisher-Exact test and Chi-Square test were performed to determine differences in the probability of recurrence of CD patients. Data are presented as mean ± standard error mean. and P-values bellow 0.05 were considered as statistically significant. Differences reached statistical significance with P values<0.05 (*), <0.01 (**) and P<0.001 (***).

Supplementary figures

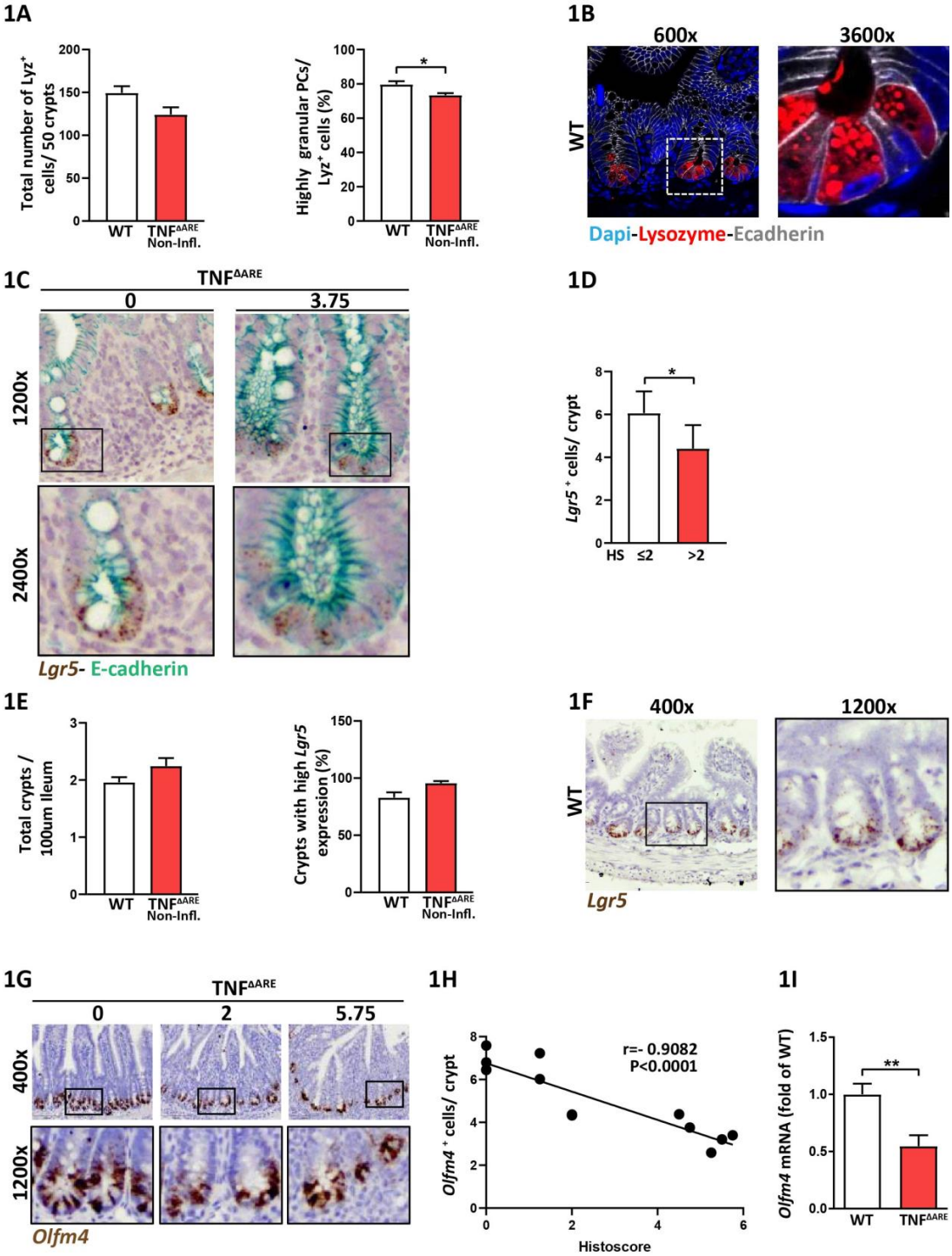

Supplementary figure 1: Inflammation but not genotype causes alterations in the ISC niche in TNF$^{\Delta ARE}$ mice

(**A, B**) Ileal tissue sections from non-inflamed TNF$^{\Delta ARE}$ and WT mice were analyzed. (**A**) Quantification of the total number of Lysozyme positive (Lyz$^+$) cells (left) and the proportion of highly granular Lyz$^+$ cells (≥2 granules). (**B**) Representative pictures of IF co-staining of Lysozyme (red) and E-cadherin (IEC borders, grey) counterstained with Dapi (nuclei, blue), including magnification showing Lyz$^+$ granules. (**C, D**) Ileal tissue sections from TNF$^{\Delta ARE}$ mice with different levels of inflammation were analyzed. (**C**) Representative pictures of *Lgr5 in situ* hybridization and IHC co-staining for E-cadherin. Numbers above indicate the respective histopathological score (HS). (**D**) Quantification of the number of *Lgr5*$^+$ cells per crypt. (**E, F**) Ileal tissue sections from non-inflamed TNF$^{\Delta ARE}$ and WT mice were analyzed. (**E**) Quantification of the number of crypts (left) and of *Lgr5 in situ* hybridization giving the proportion of crypts with high *Lgr5* expression (≥10 *Lgr5* transcripts). (**F**) Representative pictures of *Lgr5 in situ* hybridization in WT mice, including magnification. (**G, H**) Ileal tissue sections from TNF$^{\Delta ARE}$ mice with different levels of inflammation were analyzed. (**G**) Representative pictures of *Olfm4 in situ* hybridization, including magnifications; numbers indicate the respective histopathological score (HS). (**H**) Correlation analysis (Pearson) of the number of *Olfm4*$^+$ cells and HS. (**I**) qRT-PCR analysis of TNF$^{\Delta ARE}$ and WT mice-derived IECs for *Olfm4* (N=5). Statistics were performed by unpaired *t*-test. Bars represent mean+s.e.m. Asterisks indicate significant differences **P*<0.05, ***P*<0.01, ****P*<0.001.

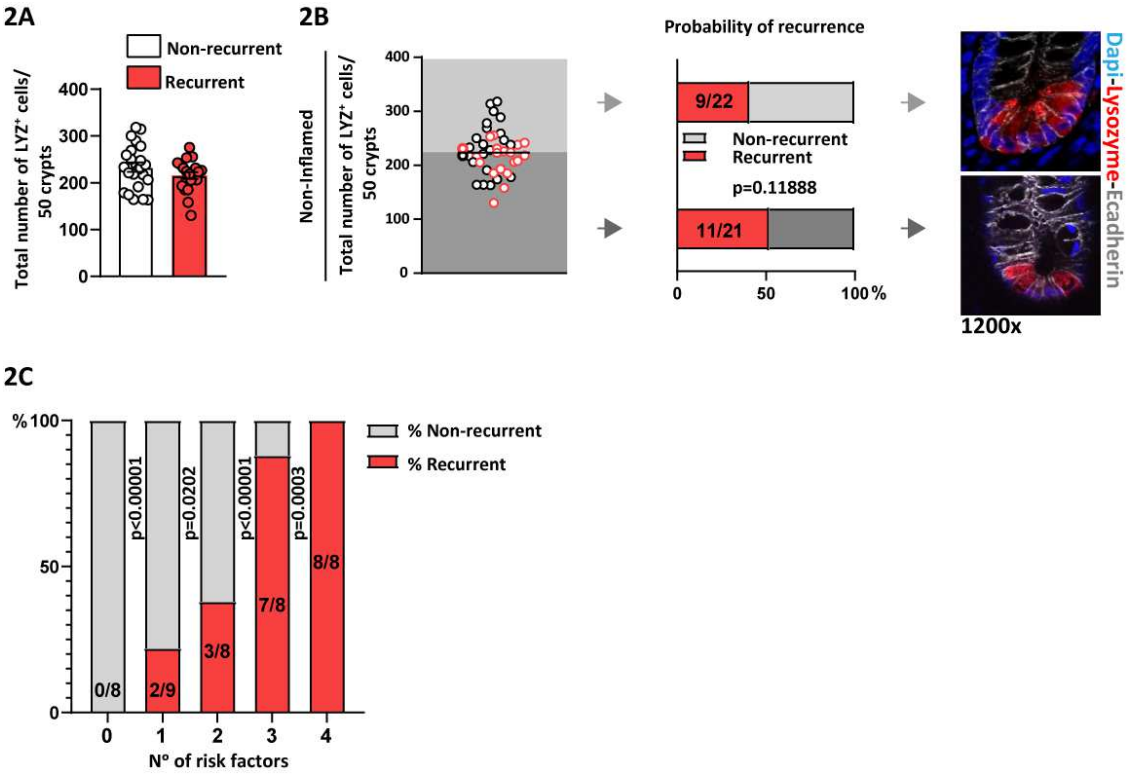

Supplementary figure 2: Risk of recurrence increases with the cumulative number of risk factors in CD patients non-inflamed at time of surgery

Ileal tissue sections classified as non-inflamed at time of surgery of CD patients undergoing resection surgery were analyzed. Tissue sections were stained for Lysozyme (LYZ) by IF and total number of LYZ positive cells in crypts were determined. CD patients with endoscopic recurrence (Rutgeerts score ≥i2) 6-12 months after surgery were compared to CD patients not experiencing recurrence. (**A**) overall comparison of recurrent versus non-recurrent patients for the total number of LYZ$^+$ cells. Statistics were performed by unpaired *t*-test. Bars represent mean+s.e.m. (**B**) From left to right: distribution of the total number of LYZ$^+$ cells among recurrent (red circles) and non-recurrent (black circles) CD patients with median indicated; probability of CD patients to experience recurrence if above or below the median for the respective marker; representative pictures showing sections from CD patients above or below median, IF co-staining of Lysozyme (red) and E-cadherin (IEC borders, grey) counterstained with Dapi (nuclei, blue). Chi-square test was used to determine significance. (**C**) Total numbers of highly granular PCs (below median), PCs in upper crypt (above median), highly *Lgr5* expressing crypts (below median) and *Lgr5* expression in upper crypts (above median) were assigned as risk factors resulting in a possible score from 0-4 for recurrent CD patients. The probability of CD patients non-inflamed at time of surgery to experience recurrence with indicated numbers of risk factors is shown. Statistical analyses were performed via Fisher-Exact test. Differences were considered statistically significant for $P<0.05$.

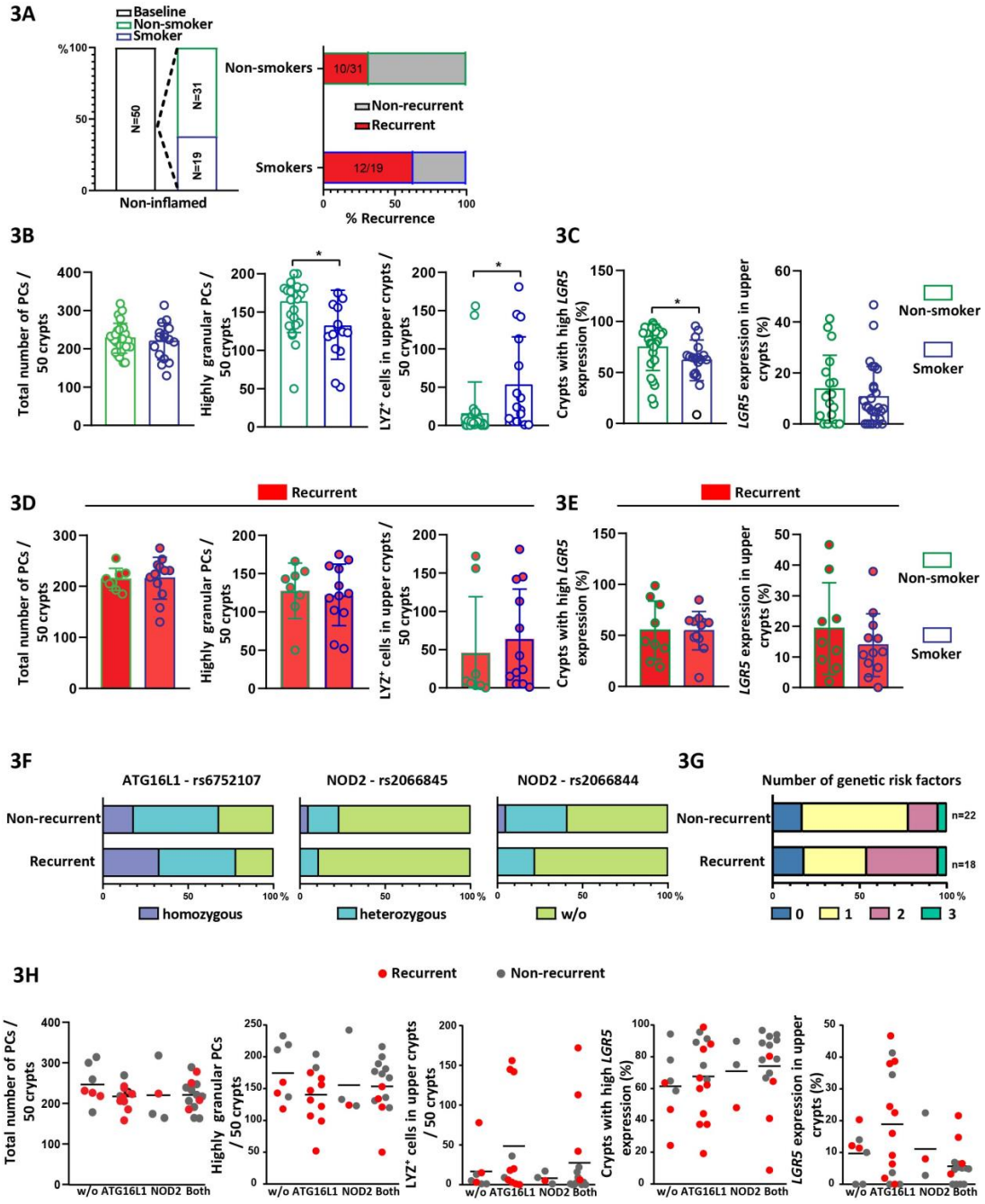

Supplementary figure 3: Smoking and genetic risk factors have no additional impact on ISC niche risk factors

Data from ileal tissue sections of CD patients undergoing resection surgery were analyzed for the smoking status of CD patients. (**A**) Overview of CD patient numbers and smoking status for baseline and endoscopic follow-up disease classification. (**B, C**) Total numbers of LYZ$^+$ cells, numbers of highly granular LYZ$^+$ cells (≥2 granules), numbers of LYZ$^+$ cells in upper crypt, proportion of crypts with high *LGR5* expression (≥15 *LGR5* transcripts), and proportion of crypts with *LGR5* expression in upper crypt are depict for all patients regardless endoscopic follow-up disease classification according to the smoking. (**D, E**) The same readouts as in (**B**) and (**C**) are depict for patients experiencing endoscopic recurrence according to the smoking

status, showing no additional impact of smoking on the risk factors analyzed. (**F**) Distribution of CD-associated SNPs ATG16L1 rs6752107 and NOD2 rs2066845 or rs2066844 among recurrent and non-recurrent CD patients. (**G**) Numbers of risk alleles in recurrent and non-recurrent CD patients. (**H**) The same readouts as in (**B**) and (**C**) are depict according to patients´ genetics. Dots representing patients experiencing recurrence are given in red. No differences were found between genotypes for the risk factors analyzed. Statistical analyses were performed via unpaired *t*-test. Bars represent mean+s.e.m. Asterisks indicate significant differences $*P<0.05$.

Khaloian S, *et al. Gut* 2020;0:1–13. doi: 10.1136/gutjnl-2019-319514

4

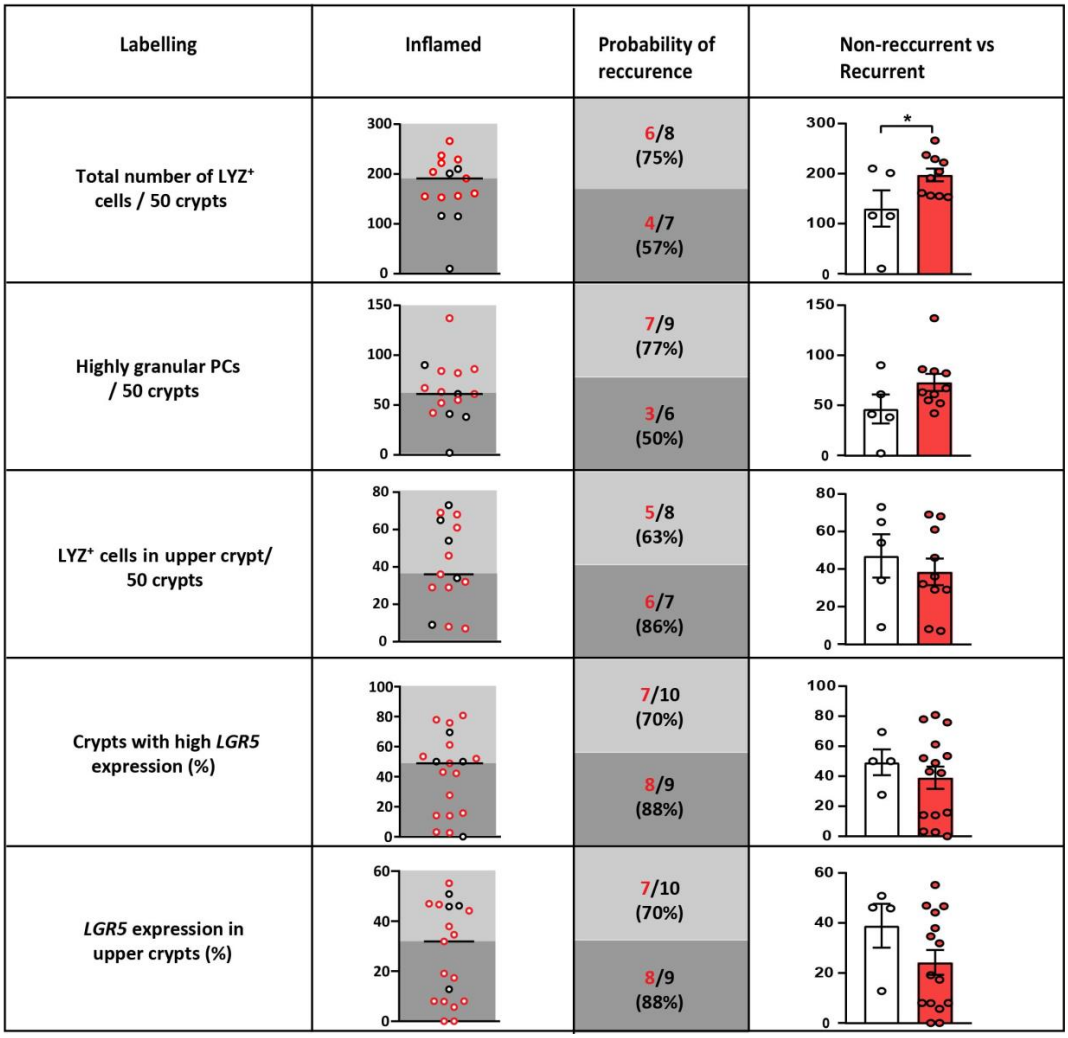

Supplementary figure 4: Paneth cell phenotype and *LGR5* expression pattern are not predictive for disease recurrence in inflamed CD patients

Ileal tissue sections classified as inflamed at time of surgery of CD patients undergoing resection surgery were analyzed. Tissue sections were stained for Lysozyme (LYZ) by IF and for *LGR5* by *in situ* hybridization, respectively, and expression patterns were quantified. From top to bottom: total numbers of LYZ$^+$ cells, numbers of highly granular LYZ$^+$ cells (≥2 granules), numbers of LYZ$^+$ cells in upper crypt, proportion of crypts with high *LGR5* expression (≥15 *LGR5* transcripts), and proportion of crypts with *LGR5* expression in upper crypt were determined. CD patients with endoscopic recurrence (Rutgeerts score ≥i2) 6-12 months after surgery were compared to CD patients not experiencing recurrence. From left to right: distribution of the respective marker among recurrent (red circles) and non-recurrent (black circles) CD patients with median indicated; probability of CD patients to experience recurrence if above or below the median for the respective marker; overall comparison of recurrent versus non-recurrent patients for the respective marker. Statistics were performed by unpaired *t*-test. Bars represent mean+s.e.m. Asterisks indicate significant differences *P<0.05.

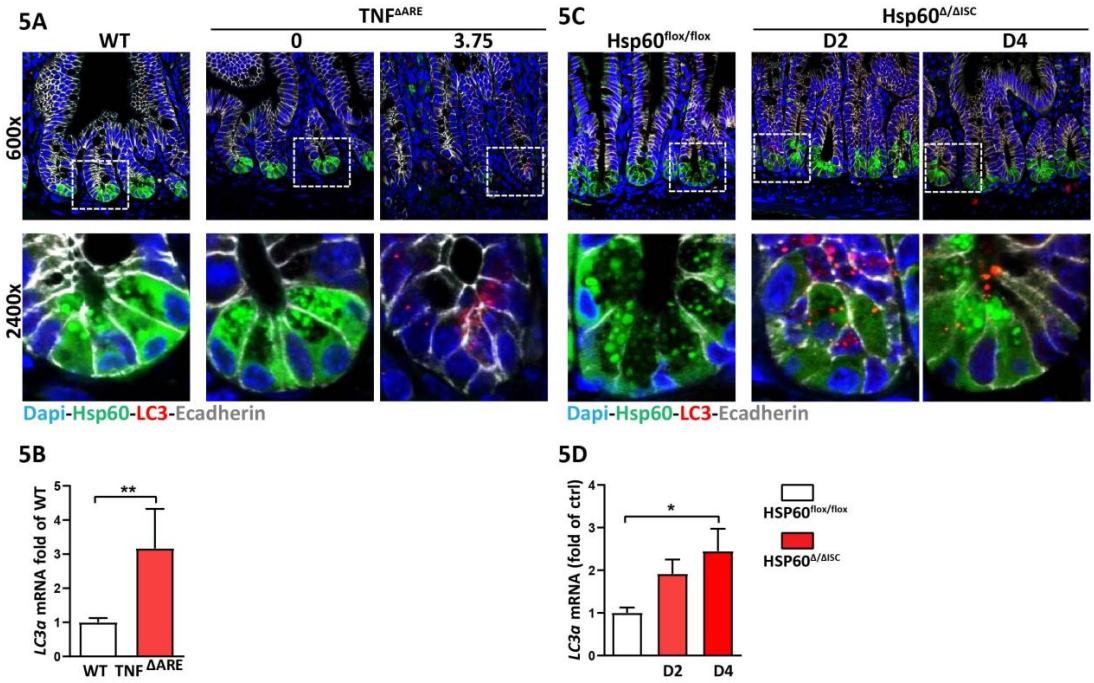

Supplementary figure 5: Induction of autophagy in mouse models of inflammation and mitochondrial dysfunction

Representative pictures of IF co-staining of LC3 (red), Hsp60 (green) and E-cadherin (IEC borders, grey) counterstained with Dapi (nuclei, blue) and qRT-PCR analysis of LC3a mRNA levels. (**A**) Ileal tissue sections from TNF$^{\Delta ARE}$ mice and WT littermates. Numbers above indicate the respective histopathological score (HS) (**B**) Primary isolated crypts from TNF$^{\Delta ARE}$ mice and WT littermates (N=5). (**C**) Ileal tissue sections from Hsp60$^{\Delta/\Delta ISC}$ and Hsp60$^{flox/flox}$ mice at D2 and D4 after end of tamoxifen treatment. (**D**) IEC isolates from Hsp60$^{\Delta/\Delta ISC}$ and Hsp60$^{flox/flox}$ mice. Statistical analysis was performed via unpaired *t*-test or One-way analysis of variance (ANOVA) followed by Tukey test when comparing more than two groups. Bars represent mean+s.e.m. Asterisks indicate significant differences **P*<0.05, ***P*<0.01.

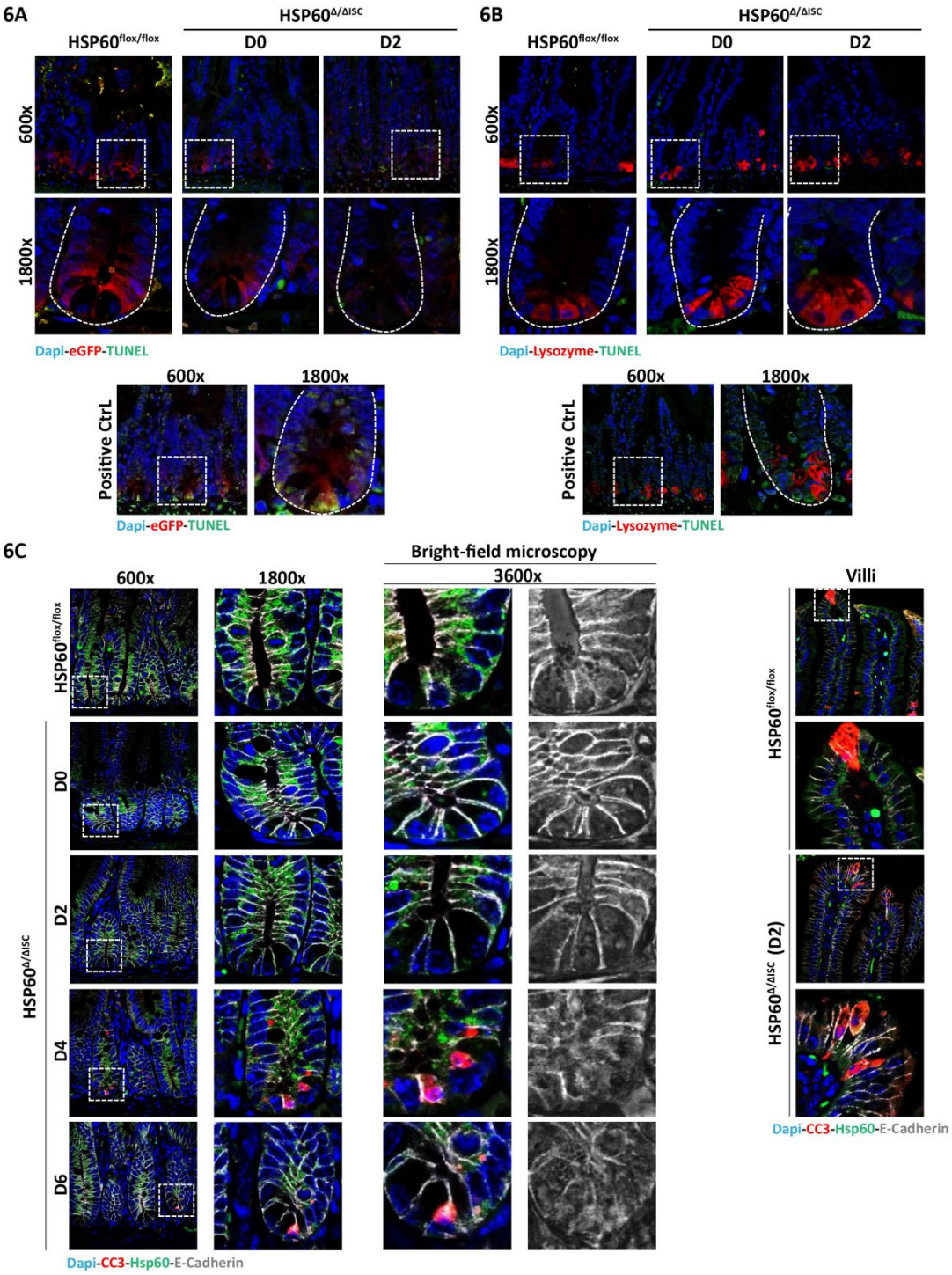
6A
HSP60flox/flox
HSP60Δ/ΔISC
D0
D2
600x
1800x
Dapi-eGFP-TUNEL
Positive CtrL
Dapi-eGFP-TUNEL
6B
Dapi-Lysozyme-TUNEL
Dapi-Lysozyme-TUNEL
6C
Bright-field microscopy
3600x
Villi
D4
D6
HSP60Δ/ΔISC (D2)
Dapi-CC3-Hsp60-E-Cadherin
Dapi-CC3-Hsp60-E-Cadherin

Supplementary figure. 6: Loss of Hsp60 in intestinal stem cells induces apoptosis subsequently to loss of *Lgr5*-positive cells

Ileal tissue sections from Hsp60$^{\Delta/\Delta ISC}$ mice and Hsp60$^{flox/flox}$ controls were analyzed at different time points after end of tamoxifen treatment. (**A, B**) IF co-staining of eGFP (**A**, red, indicating *Lgr5* expressing cells) or lysozyme (Lyz) (**B**, red, indicating Paneth cells) and TUNEL staining (green, indicating apoptotic cells), for the indicated time-points, including magnifications. Lower panel: positive control for TUNEL assay (tissue sections treated with DNaseI), overlap of eGFP and TUNEL staining is indicated in yellow. (**C**) IF co-staining of cleaved caspase 3 (red, indicating apoptotic cells), Hsp60 (green) and E-cadherin (IEC borders, grey) counterstained with Dapi (nuclei, blue) in crypts; right side: magnifications including bright field images. Right panel: CC3 staining in villi, serving as a positive control.

Khaloian S, *et al. Gut* 2020;0:1–13. doi: 10.1136/gutjnl-2019-319514

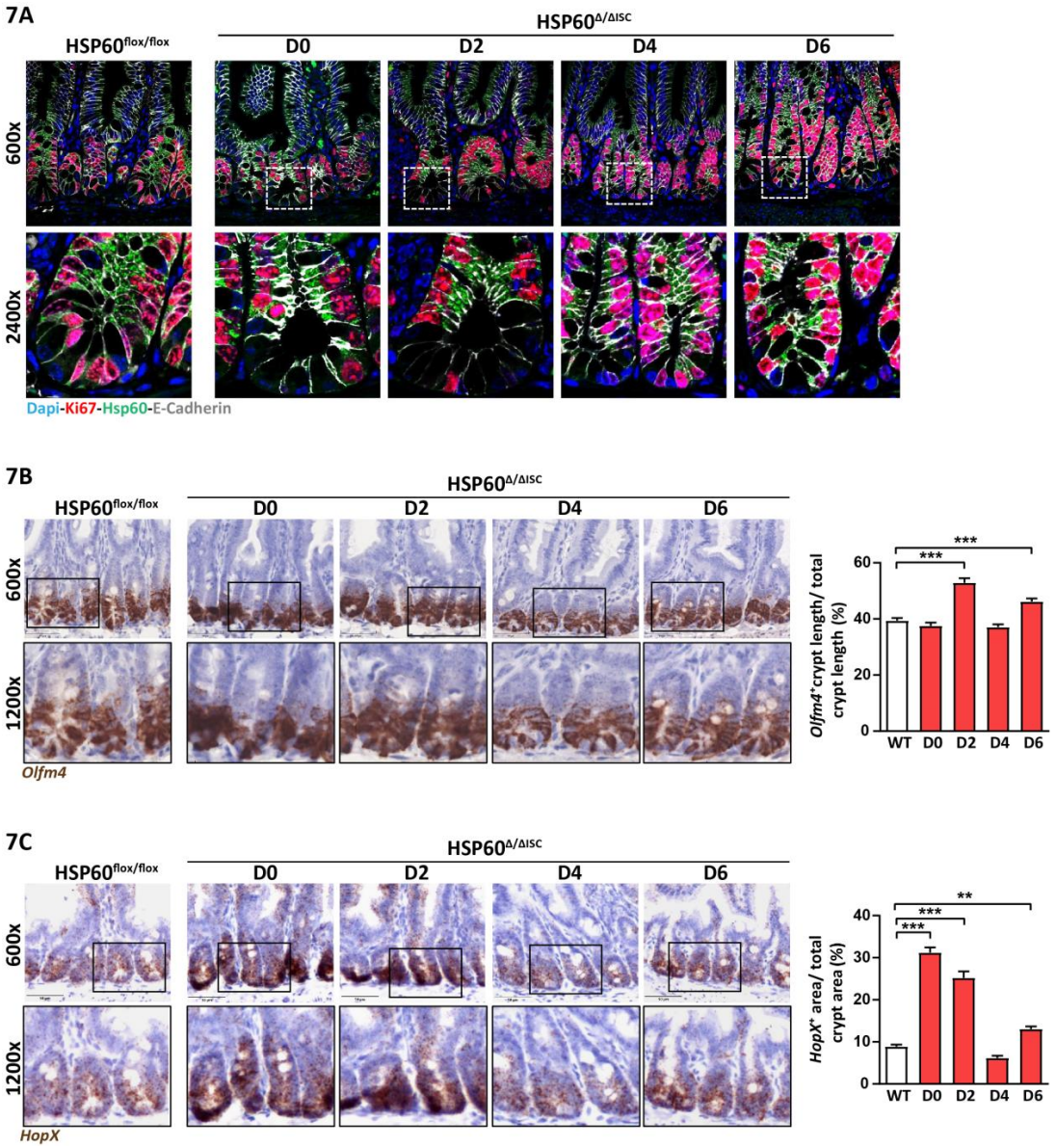

Supplementary figure 7: Hsp60 negative cells do not proliferate and remain in the crypt base, but crypts remain *Olfm4* and *Hopx* positive

Small intestinal tissue sections from Hsp60$^{\Delta/\Delta ISC}$ mice and Hsp60$^{flox/flox}$ controls were analyzed at different time points after end of tamoxifen treatment. (**A**) IF co-staining of Hsp60 (green), E-cadherin (IEC borders, grey) and Ki67 (proliferation, red) in ileal tissue sections. Dapi stains the nuclei in blue. (**B, C**) Left: representative pictures of *Olfm4* (**B**) and *Hopx* (**C**) *in situ* hybridization, including magnifications. (B) Right: quantification of the distance of the most upper *Olfm4* positive cell to the crypt ground normalized to crypt length (**C**) Right: quantification of the area positive for *Hopx* normalized to crypt area (N=3). Statistical analysis was performed via One-way analysis of variance (ANOVA) followed by Tukey test. Bars represent mean+s.e.m. Asterisks indicate significant differences **P*<0.05, ***P*<0.01, ****P*<0.001.

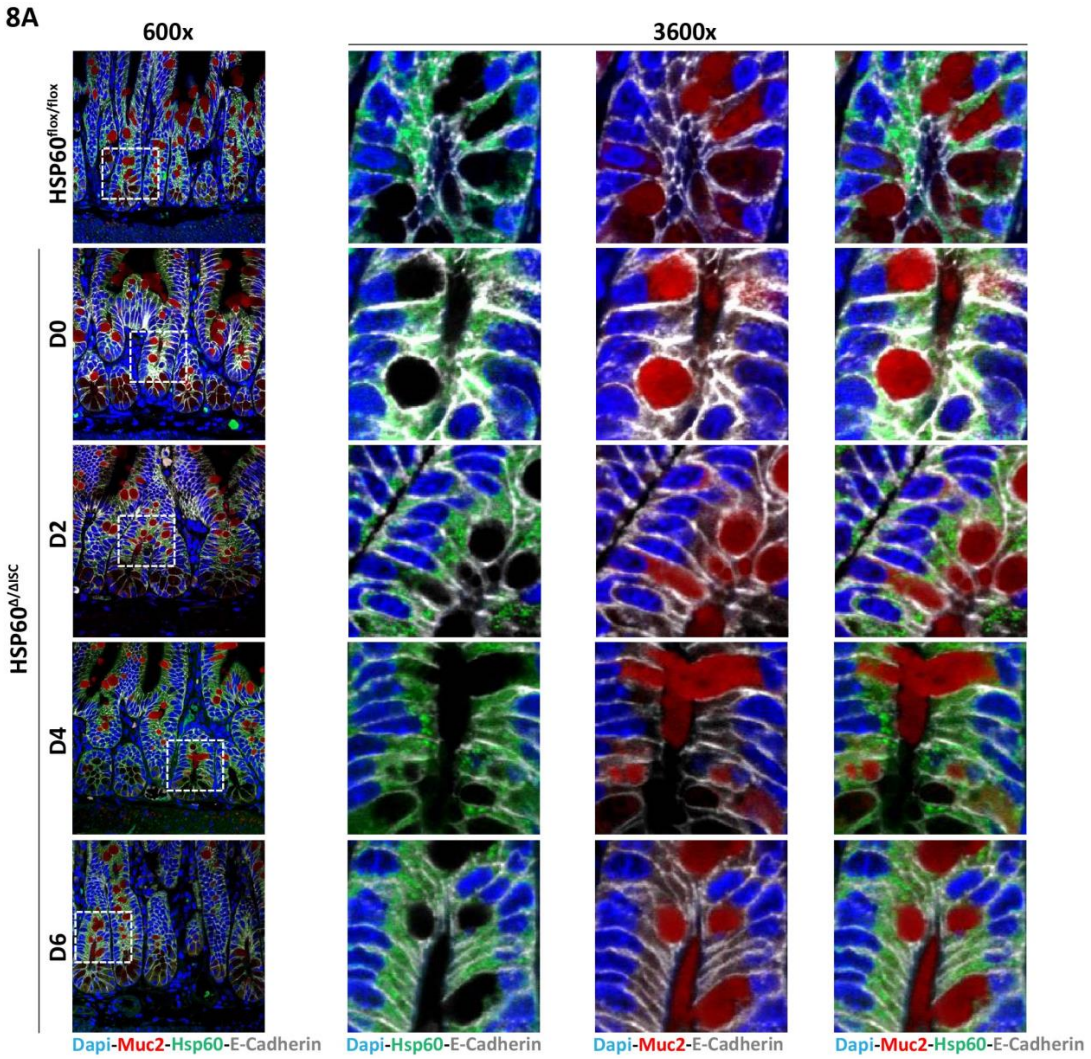
8A
600x
3600x
HSP60flox/flox
HSP60Δ/ΔISC
D0
D2
D4
D6
Dapi-Muc2-Hsp60-E-Cadherin
Dapi-Hsp60-E-Cadherin
Dapi-Muc2-E-Cadherin
Dapi-Muc2-Hsp60-E-Cadherin

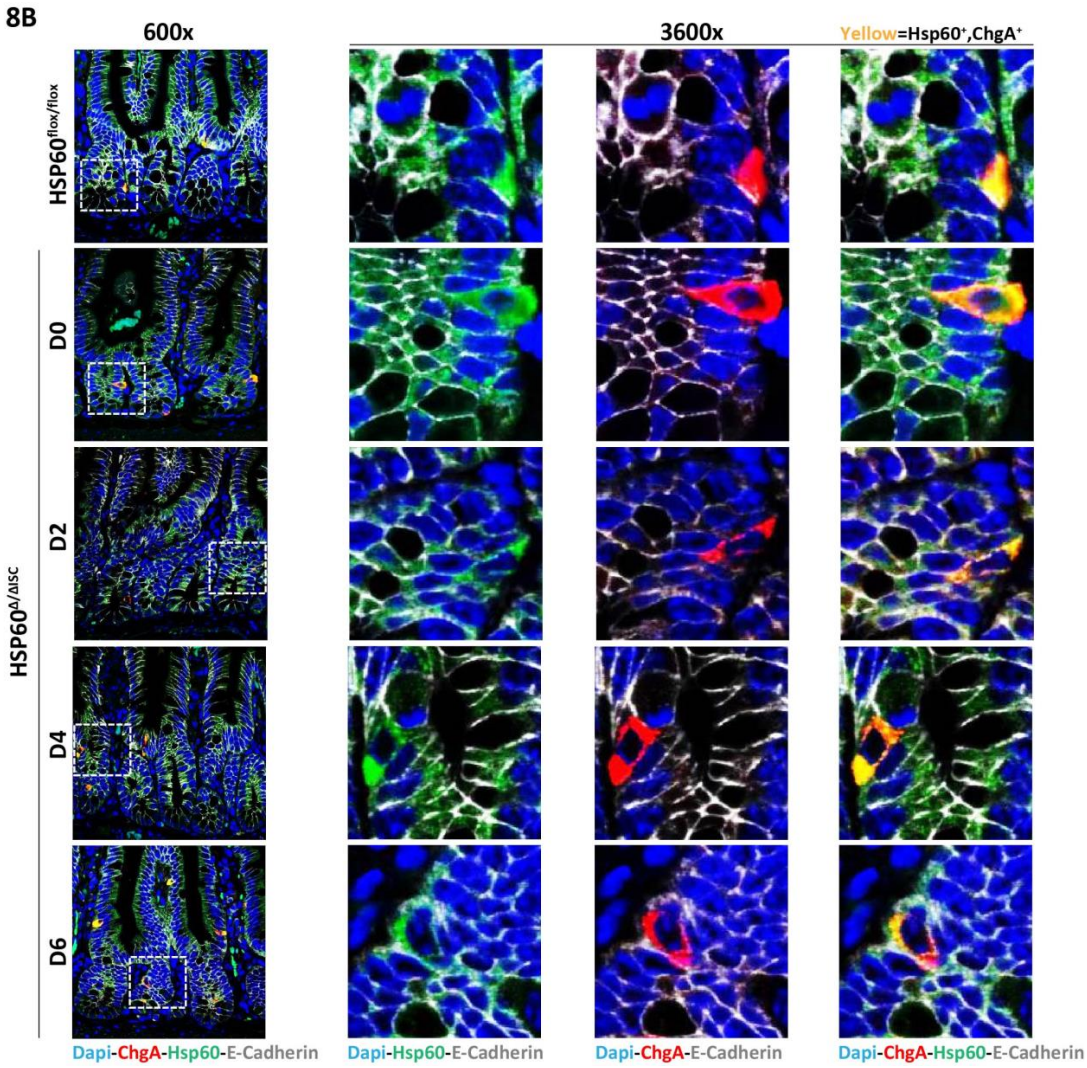
8B
600x
3600x
Yellow=Hsp60+,ChgA+
HSP60flox/flox
HSP60Δ/ΔISC
D0
D2
D4
D6
Dapi-ChgA-Hsp60-E-Cadherin
Dapi-Hsp60-E-Cadherin
Dapi-ChgA-E-Cadherin
Dapi-ChgA-Hsp60-E-Cadherin

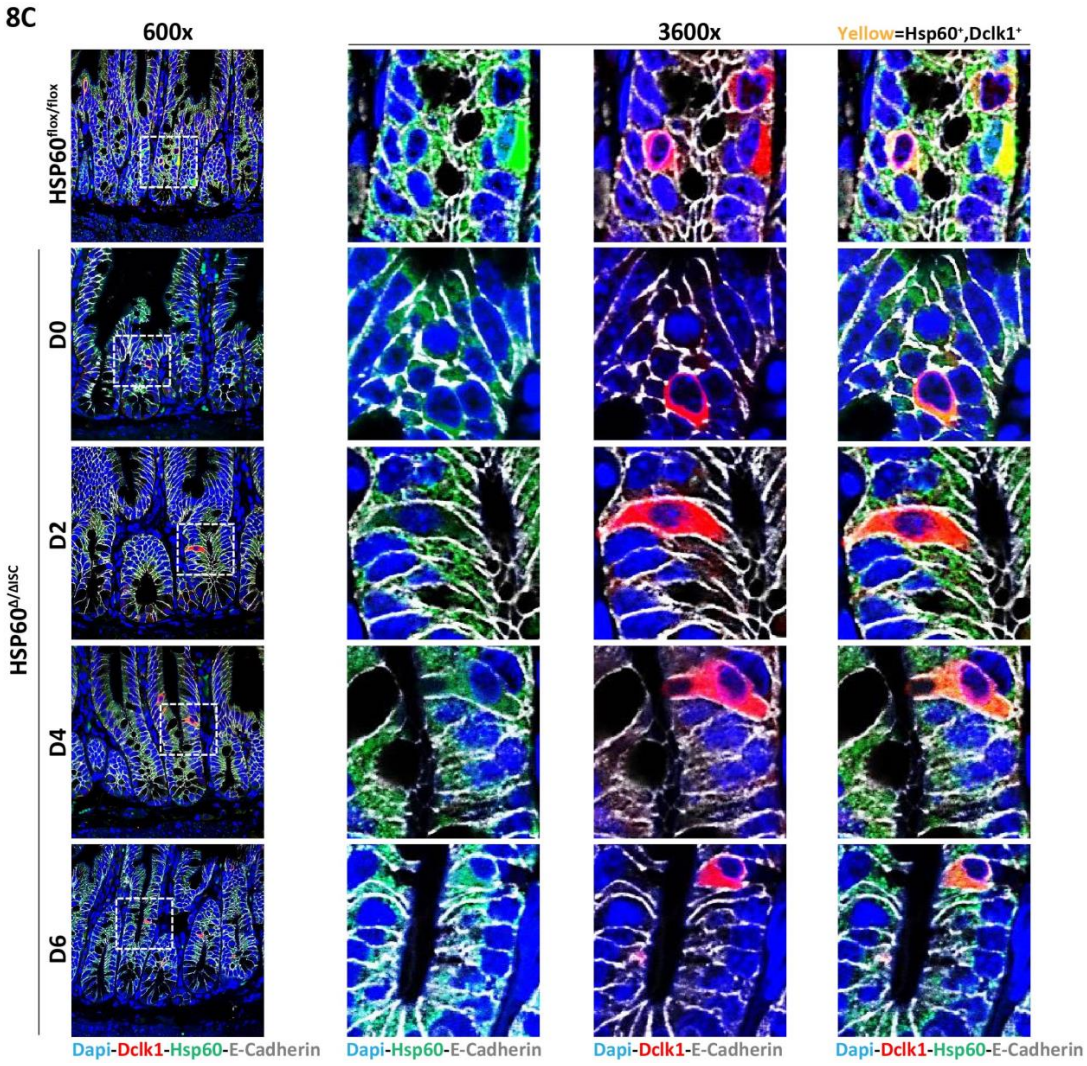

Supplementary figure 8: Hsp60 negative cells do not give rise to goblet cells, enteroendocrine cells or tuft cells

Ileal tissue sections from $Hsp60^{\Delta/\Delta ISC}$ mice and $Hsp60^{flox/flox}$ controls were analyzed at different time points after end of tamoxifen treatment. IF co-staining of Hsp60 (green), E-cadherin (IEC borders, grey) and (**A**) Muc2 (goblet cells, red), (**B**) ChgA (enteroendocrine cells, red), (**C**) Dclk1 (tuft cells) (red). Dapi stains the nuclei in blue. Muc2, ChgA and Cclk1 positive cell remain Hsp60 positive throughout the experiment.

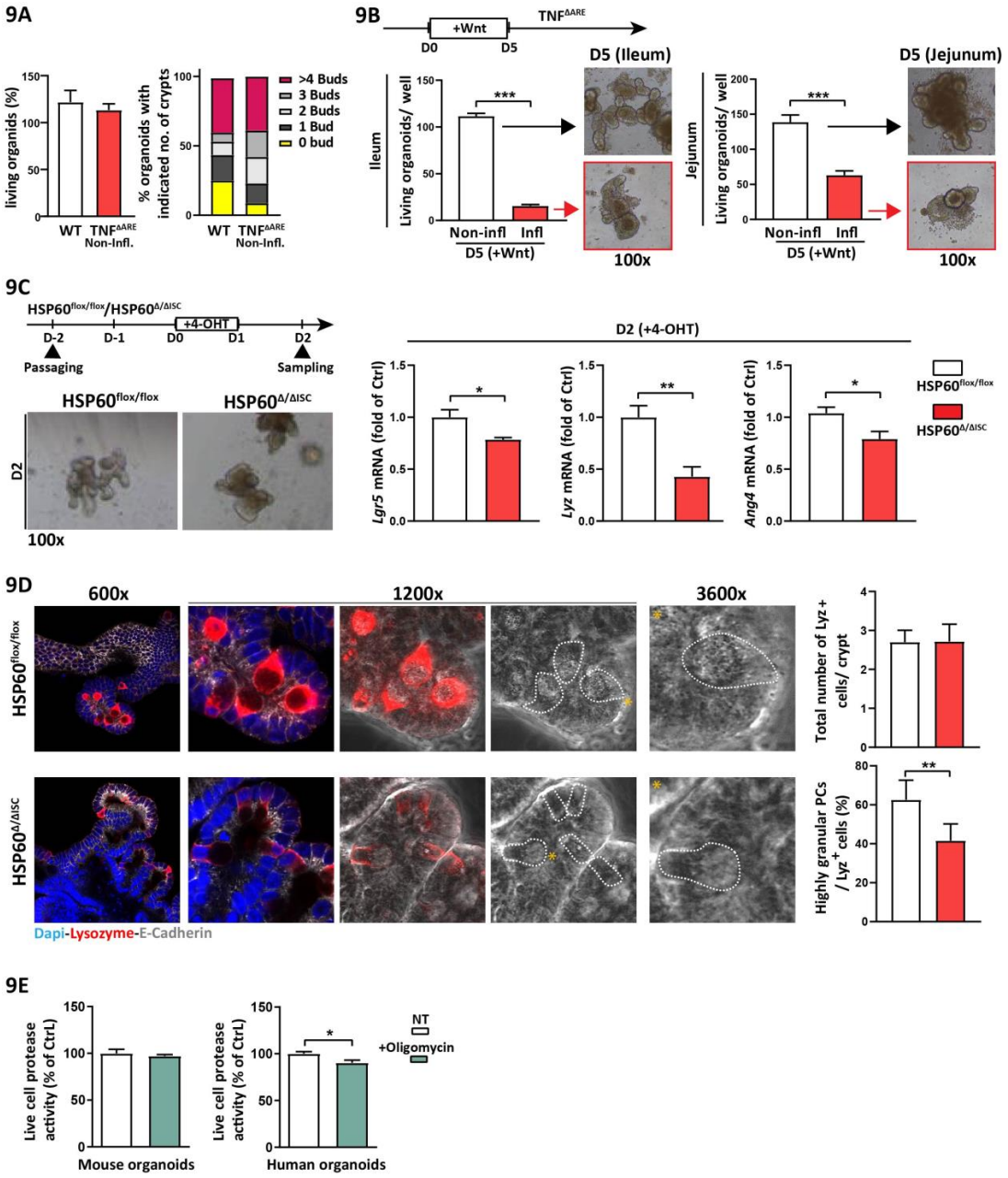

Supplementary figure 9: Wnt factor supplementation does not rescue growth of organoids derived from inflamed TNF$^{\Delta ARE}$ mice

(**A**) Growth characteristics of ileal organoids derived from non-inflamed TNF$^{\Delta ARE}$ mice and WT littermates. Left: proportion of living organoids; right: quantification of *de novo* crypt formation (budding) at day 5 of *ex vivo* culture. (**B**) Ileal (left) and jejunal (right) crypts derived from non-inflamed and inflamed TNF$^{\Delta ARE}$ mice were cultured in commercially available medium containing Wnt factors (Intesticult) for 5 days. Proportion of living organoids and representative bright field pictures are shown. (**C**) Organoids derived *Hsp60*$^{flox/flox}$ mice were treated with tamoxifen to induce ISC-specific Hsp60 loss and sampled 2 days later. Tamoxifen treated Cre negative organoids served as control. Left: representative bright field pictures; Right: qRT-PCR analysis of *Lgr5* and genes involved in PC function (N=6). (**D**) Representative pictures of IF

co-staining for Lysozyme (red) and E-cadherin (IEC borders, grey) counterstained with Dapi (nuclei, blue), including bright field pictures. Dotted lines indicate cell borders of Lyz positive (Lyz^+) cells; asterisks indicate Lyz^+ cells magnified in the pictures on the right side; Right: quantification of Lyz^+ cell numbers per crypt (upper graph) and the proportion of highly granular (≥2 granules) Lyz^+ cells (lower graph). (**E**) Measurement of living cells in murine (WT, left) and human (right) organoid cultures after treatment with oligomycin for 24h (N≥3). Statistical analysis was performed via unpaired *t*-test. Bars represent mean+s.e.m. Asterisks indicate significant differences $*P<0.05$, $**P<0.01$, $***P<0.001$.

Khaloian S, *et al. Gut* 2020;0:1–13. doi: 10.1136/gutjnl-2019-319514

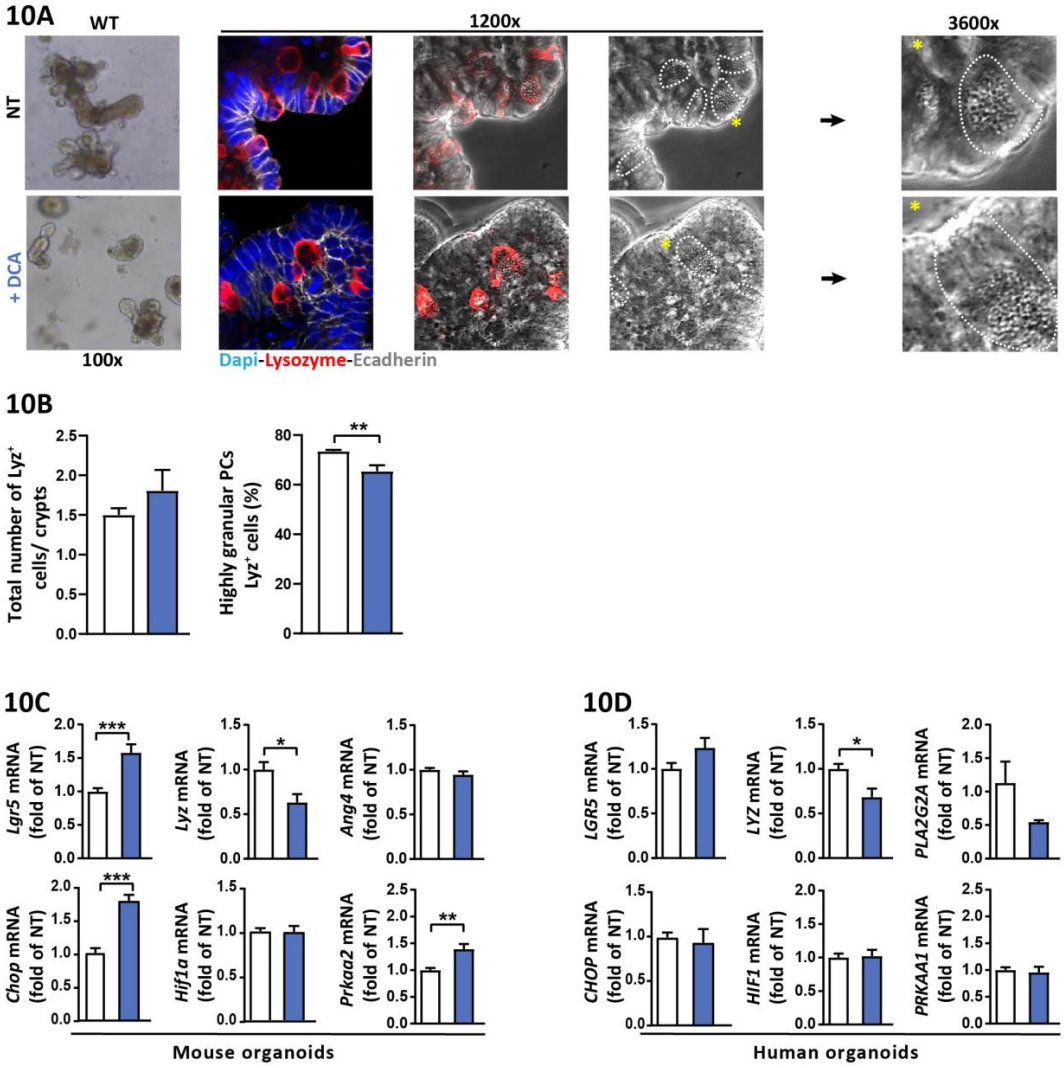

Supplementary figure 10: DCA treatment of WT ileal organoids

Ileal organoids derived from WT mice were treated with DCA for 24h. (**A**) Left: bright field and IF co-staining of Lyz (red) and E-cadherin (IEC borders, grey) counterstained with Dapi (nuclei, blue). Dotted lines indicate cell borders of Lyz positive (Lyz$^+$) cells; asterisks indicate Lyz$^+$ cells magnified in the pictures on the right side. (**B**) Quantification of Lyz$^+$ cell numbers per crypt (left graph) and the proportion of highly granular (≥2 granules) Lyz$^+$ cells (right graph). (**C**) qRT-PCR analysis of intestinal organoids for *Lgr5* and Paneth cell function-associated genes (upper panel) and for genes associated with mitochondrial signaling (lower panel, N=6). (**D**) Same analysis as in (**C**) for human organoids derived from the small intestine and treated with DCA for 24h (N=6). Statistical analysis was performed via unpaired *t*-test. Bars represent mean+s.e.m. Asterisks indicate significant differences **P*<0.05, ***P*<0.01, ****P*<0.001.

Supplementary tables

Table S1. **Patients' characteristics at time of surgery**.

Total number of patients included	**n=70**
Men	28 (40%)
Median age (y, IQR)	31.7 (26.4-44.0)
Age at Crohn's Disease diagnosis (Montreal classification)	
- ≤16 years (A1)	5 (7%)
- 17 - 40 years (A2)	56 (80%)
- >40 years (A3)	9 (13%)
Median disease duration (y, IQR)	6.7 (1.8-12.5)
Median time between resection and colonoscopy (mo, IQR)	6.7 (6.1-8.4)
Smoking	
- Active smoker	23 (33%)
- Smoking cessation at surgery	6 (9%)
- Non-smoker	41 (58%)
Previous intestinal resection	13 (19%)
Number of previous resection(s)	
– 0	57 (82%)
– 1	7 (10%)
– 2	3 (4%)
– 3	3 (4%)
Surgical indication	
– Stricturing complication	47 (67%)
– Penetrating complication	22 (31%)
– Failure of drug therapy	1 (2%)
Anoperineal lesion	13 (19%)
Extra-digestive symptoms	
- Joint manifestations	18 (26%)
- Skin manifestations	6 (9%)
- Eye manifestations	2 (3%)
Previous exposure to anti-TNF therapy	42 (60%)
Anti-TNF therapy within 3 months before surgery	29 (41%)
Previous exposure to thiopurines	53 (76%)
Thiopurines within 3 months before surgery	20 (29%)
Ileal resection margin inflamed	20 (29%)

Table S2. **Primary antibodies used in the study**.

Primary antibodies:	**Species:**	**Company:**	**Dilution:**
Anti-CC3	Rabbit	Cell signaling Technology, Danvers, MA	1:100
Anti-E-cadherin	Mouse	Abcam, Cambridge, UK	1:300
Anti-GFP (XP)	Rabbit	Cell signaling Technology, Danvers, MA	1:200
Anti-HSP60	Goat	Santa Cruz Biotechnology, Santa Cruz, CA	1:200
Anti-Lysozyme	Rabbit	Dako, Agilent, Santa Clara	1:1000
Anti-Chromogranin A	Rabbit	Abcam, Cambridge, UK	1:100
Anti-Dclk1	Rabbit	Biomol, Hamburg, Germany	1:100
Anti-Ki67	Rabbit	Cell signaling Technology, Danvers, MA	1:400
Anti-MAP LC3α/ß	Goat	Santa Cruz Biotechnology, Santa Cruz, CA	1:200
Anti-Muc2	Rabbit	BioTechne, Wiesbaden, Germany	1:200
Anti-PKR (M-515)	Rabbit	Santa Cruz Biotechnology, Santa Cruz, CA	1:100

Table S3. **Secondary antibodies used in the study**

Secondary antibodies:	**Company:**	**Dilution:**
HRP conjugated mouse anti goat IgG	Dianova, Hamburg, Germany	1:300
HRP conjugated donkey anti rabbit IgG	Dianova, Hamburg, Germany	1:300
Alexa Fluor donkey anti goat 488	Life Technologies, Carlsbad, CA	1:200
Alexa Fluor donkey anti rabbit 546	Life Technologies, Carlsbad, CA	1:200
Alexa Fluor donkey anti mouse 647	Life Technologies, Carlsbad, CA	1:200
Dapi	Sigma- Aldrich, Taufkirchen, Germany	1:1000

Khaloian S, *et al. Gut* 2020;0:1–13. doi: 10.1136/gutjnl-2019-319514

Table S4. **Primer sequences and probes for qRT-PCR**

Target genes Mouse:	**Forward primer (L):**	**Reverse primer (R):**	**Probe:**
Ang4	ccccagttggaggaaagc	cgtaggaatttttcgtacctttca	106
Atf5	tttttatgaagaggaataagatgaggt	ggaggctgcaccaacaat	16
Chop	cgacagagccagaataacagc	aagggttagacggagccagt	91
CoxIV	tcactgcgctcgttctgat	cgatcgaaagtatgagggatg	7
Defa5	ttttgggacctgcagaaatc	tggttgttgaccatccttgtt	84
Dll4	aggtgccacttcggttacac	gggagagcaaatggctgata	106
Grp78	ctgaggcgtatttgggaaag	tcatgacattcagtccagcaa	105
Hif1a	gcactagacaaagttcacctgaga	cgctatccacatcaaagcaa	95
Hprt	tcctcctcagaccgctttt	cctggttcatcatcgctaatc	95
Hsp10	ggcccgagttcagagtcc	tgtcaaagagcggaagaaactt	77
Hsp60	tcttcaggttgtggcagtca	cccctcttctccaaacactg	1
Lc3a	gaccagcaccccagtaagat	tgggaccagaaacttggtct	27
Lgr5	cttcactcggtgcagtgct	cagccagctaccaaataggtg	60
Lyz1	ggcaaaaccccaagatctaa	tctctcaccaccctctttgc	46
Olfm4	gaaattcgagagagagttttctaagg	gacctctactcggaccgtca	92
Otc	gctgtcatggtatccctgct	tttccttttgacaggcatca	99
Pdha	catcgttggagctcaggtg	cgccgtataatgtcaaacagac	15
Prkaa2	cagagcaaagcgtgtgacat	ttcttcttactcgaagatggtatgc	41
Trb3	gtcgctttgtcttcagcaact	tcatctgatccagtcatcacg	67
Yy1	ctggagaaaagccctttcag	gtcgaaggggcacacatag	94

Target genes Human:	**Forward primer (L):**	**Reverse primer (R):**	**Probe:**
CHOP	Cagagctggaacctgaggag	tgtttatggctgctttggtg	9
DLL1	gtggggagaaagtgtgcaa	tcacaaaatccatgctgctc	20
HIF1A	gaacctgatgctttaactttgct	tgctggtcatcagtttctgtg	28
HPRT1	tgatagatccattcctatgactgtaga	caagacattcttccagttaaagt	22
LGR5	accagactatgcctttggaaac	tcccagggagtggattctatt	78
LYZ	ccgctactggtgtaatgatgg	catcagcgatgttatcttgcag	68
PLA2G2A	aaatttctgagctacaagtttagcaac	ttatcacactcacacagttgacttct	32
PRKAA1	ctgatattttcatggtgatggaat	gacgccgactttctttttca	63

References

1 Berger E, Rath E, Yuan D, Waldschmitt N, Khaloian S, Allgauer M*, et al.* Mitochondrial function controls intestinal epithelial stemness and proliferation. Nat Commun 2016;**7**:13171.
2 Harder U, Koletzko B, Peissner W. Quantification of 22 plasma amino acids combining derivatization and ion-pair LC-MS/MS. J Chromatogr B Analyt Technol Biomed Life Sci 2011;**879**:495-504.
3 Gucciardi A, Pirillo P, Di Gangi IM, Naturale M, Giordano G. A rapid UPLC-MS/MS method for simultaneous separation of 48 acylcarnitines in dried blood spots and plasma useful as a second-tier test for expanded newborn screening. Anal Bioanal Chem 2012;**404**:741-51.
4 Erben U, Loddenkemper C, Doerfel K, Spieckermann S, Haller D, Heimesaat MM*, et al.* A guide to histomorphological evaluation of intestinal inflammation in mouse models. Int J Clin Exp Pathol 2014;**7**:4557-76.
5 Auzolle C, Nancey S, Tran-Minh ML, Buisson A, Pariente B, Stefanescu C*, et al.* Male gender, active smoking and previous intestinal resection are risk factors for post-operative endoscopic recurrence in Crohn's disease: results from a prospective cohort study. Aliment Pharmacol Ther 2018;**48**:924-32.
6 Hammoudi N, Cazals-Hatem D, Auzolle C, Gardair C, Ngollo M, Bottois H*, et al.* Association Between Microscopic Lesions at Ileal Resection Margin and Recurrence After Surgery in Patients With Crohn's Disease. Clin Gastroenterol Hepatol 2019.
7 Zietek T, Rath E. Chapter 3 - Intestinal organoids: Mini-guts grown in the laboratory. In: Davies JA, Lawrence ML, eds. Organs and Organoids: Academic Press, 2018:43-71.